Applied Catalysis B: Environmental 342 (2024) 123405

Contents lists available at ScienceDirect

Applied Catalysis B: Environmental

journal homepage: www.elsevier.com/locate/apcatb

Sustainable coke-resistant Ca-Al nano-sized catalyst for cogenerating hydrogen and high-value liquid fuels via pyrolysis catalytic steam reforming reaction of the polystyrene-phenol mixture

Walid Nabgan [a,*,1], Mohd Zahid Ansari [b,*,1], Muhammad Ikram [c,*], Hasan Alqaraghuli [d], L. Parashuram [e], Thuan Van Tran [f,g], Mohammed A. Amin [h], Tuan Amran Tuan Abdullah [g], Ridha Djellabi [a], Francisco Medina [a], Aishah Abdul Jalil [g]

[a] Departament d'Enginyeria Química, Universitat Rovira i Virgili, Av Països Catalans 26, 43007, Tarragona, Spain
[b] School of Materials Science and Engineering, Yeungnam University, 280 Daehak-Ro, Gyeongsan, Gyeongbuk 38541, the Republic of Korea
[c] Solar Cell Applications Research Lab, Department of Physics, Government College University Lahore 54000, Punjab, Pakistan
[d] Faculty of Electrical Engineering, Universiti Teknologi Malaysia, 81310 Skudai, Johor, Malaysia
[e] Department of Chemistry, Nitte Meenakshi Institute of Technology, Yelahanka, Bangalore 560064, India
[f] Institute of Applied Technology and Sustainable Development, Nguyen Tat Thanh University, 300A Nguyen Tat Thanh, District 4, Ho Chi Minh City 755414, Viet Nam
[g] Faculty of Chemical and Energy Engineering, Faculty of Engineering, Universiti Teknologi Malaysia, 81310 Skudai, Johor, Malaysia
[h] Department of Chemistry, College of Science, Taif University, P.O. Box 11099, Taif 21944, Saudi Arabia

ARTICLE INFO

Keywords:
Free-noble-metal
Hydrogen
Liquid fuel
Polystyrene
Phenol

ABSTRACT

The production of synthetic plastics, particularly polystyrene (PS), has had a significant impact on humanity and has led to an increase in global waste. Since conventional treatment methods cannot effectively recycle these materials, this study aimed to find a solution by valorizing polystyrene waste and phenol through an in-situ pyrolysis-catalytic steam reforming reaction utilizing the γ-Al_2O_3 (Al) and CaO (Ca) nanomaterials for the production of hydrogen and liquid fuel. The catalysts were prepared using impregnation and hydrothermal techniques, and their physicochemical properties were characterized after being calcined and utilized. Among the catalysts used, the 2Ca3Al nanocatalyst had high performance due to its high surface area, uniformly distributed Ca and Al alloy, surface hydroxyl groups, and oxygen vacancies. At 700 ^{o}C, the 2Ca3Al nanocatalyst demonstrated a phenol conversion rate and H_2 yield of 98.5 % and 92.5 %, respectively. The main compounds detected in the liquid product were tert-Butyl Hydroperoxide (TBH) and Dixanthogen.

1. Introduction

Due to the significant increase in the global population, industrial and agricultural activities, and world economy, various environmental and energy issues have emerged, including energy demand, waste accumulation, and water and air pollution. It is of the utmost importance to discover a clean energy source with a high energy level that does not contribute to climate pollution and can be produced through unconventional methods. H_2 is a promising next-generation energy carrier due to its high energy content and environmental benefits. However, most of the H_2 produced today is obtained through reforming natural gas, which makes the process energy-intensive and generates CO_2 emissions [1–3]. In addition to gaseous emissions, large amounts of solid waste, including plastic waste, are discarded into the environment [4,5]. Plastic production increased from 15 million tons in 1964 to over 300 million tons in 2017 worldwide, and the growth of plastic waste outpaces efforts to address plastic pollution. These factors have caused significant amounts of wasted plastics [6]. Emerging plastic contaminants are pervasive in aquatic ecosystems and represent severe risks to the safety of both human health and marine life. An efficient abatement technology is needed to break down organic contaminants. One of the most widely manufactured polymers is polystyrene (PS), with a demand for 1.58 million tonnes of plastics in 2019 alone in Europe. PS is among the most extensively researched polymers regarding its impacts on aquatic

* Corresponding authors.
E-mail addresses: walid.nabgan@urv.cat (W. Nabgan), zahid.smr@yu.ac.kr (M.Z. Ansari), dr.muhammadikram@gcu.edu.pk (M. Ikram).
[1] These authors contributed equally.

https://doi.org/10.1016/j.apcatb.2023.123405
Received 17 January 2023; Received in revised form 11 August 2023; Accepted 16 October 2023
Available online 20 October 2023
0926-3373/© 2023 Elsevier B.V. All rights reserved.

creatures due to its widespread usage, often in single-use goods related to food packaging [7]. Due to their loose structure and rough surface, PS is more readily exfoliated when subjected to modest mechanical stress, leading to numerous fractured spots with a size range of 20–100 m on the surface of containers [8]. PS was chosen because it is frequently used for cutlery, packaging, and insulation and is high in aromatics (74 wt %). However, only 10 % of PS produced each year is recycled, and no catalytic upcycling techniques have been used to extract the valuable aromatic. Due to the lack of strength heteroatoms like those in polyethylene terephthalate and polyester, which are breakable and hence very easy to degrade, upcycling PS is generally difficult [9]. The effect of solvents on the thermal degradation of polymers is substantial. Specifically, solvents that possess the ability to donate hydrogen atoms participate in the pyrolysis of polymers, which significantly impacts the yield and distribution of hydrocarbons. However, because the solvent must be separated by rectification after the reaction, thermal degradation in the solution may be more expensive than the solventless process. In recent years, there has been a proliferation of articles and books on the methodology and emerging trends in the pyrolysis of biopolymers into fuels [10,11]. However, the large PS molecule hinders chemical, mechanical, and thermal recycling. Pyrolysis of PS waste is followed by catalytic cracking of some liquid products when dissolved with the appropriate solvent [12]. In this investigation, phenol has been used as a solvent for PS plastic waste and as a source of H_2 generation through steam reforming reactions. Phenols are bio-oil's primary liquid waste components because they have an -OH group attached to one of the sp^2 carbon atoms of a benzene ring [13]. Bio-based phenol may be produced using various techniques using industrial waste streams and biomass resources [14].

PS is very inert and difficult to break down without special treatment due to the strong C-C and C-H bonds linking all of its atoms. Chemical recycling of PS through thermal and catalytic pyrolysis is the most promising method for transforming plastic waste because it can create small molecules of plastic waste while posing less of a threat to the environment. Dissolving PS wastes in a liquefying agent for H_2 generation may be an excellent solution for sustainable and clean energy generation and addressing plastic waste reuse issues to address these severe environmental threats. Because pyrolysis produces hydrocarbon compounds like gasoline, several publications have been published on various methods for recovering plastic wastes into chemical or petrochemical substrates [15–17]. This endeavor can simultaneously alleviate the challenges associated with energy and the environment by efficiently displacing fossil fuels. Consequently, the in-situ pyrolysis-catalytic steam reforming reaction of PS dissolved in phenol technology to cogenerate H_2 and liquid fuel is crucial for changing the global energy structure.

Sintering and fouling, attributed explicitly to carbon deposition on the active sites of catalysts, represent two significant factors leading to the deactivation of catalysts in steam reforming procedures. Notably, if solid plastics were directly introduced into a catalytic bed, coke formation may be a serious concern, as plastics are high-carbon polymer materials [18]. Therefore, tremendous effort has been made to develop various typical supported non-precious transition and noble metal catalysts such as Pd [19], Pt [20], Co [21,22], Ni [23,24], Rh [25], Fe [23] for the catalytic steam reforming of phenol. In addition to the ongoing research into non-precious metal catalysts, a new class of transition and noble metal-free catalysts has recently been developed for various reactions. As alternative reforming catalysts, these transition and noble metal-free catalysts can significantly lower the price and boost the effectiveness of the in-situ pyrolysis-catalytic steam reforming reaction [26–28]. Although these transition and noble metal-free catalysts can be amorphous or crystalline, bulk or nanostructured, or chemically modified, they are not new. However, their development has seen a sharp uptick in recent years due to the economy, industrial interest, and concerns for safety and the environment. Catalysts for phenol steam reforming and plastic waste cracking reactions need a large surface area, a larger pore structure accessible for gaseous transport, and thermal stability at high temperatures, even when steam is present. One typical candidate for such complex reactions is calcium oxide (CaO) which may trap CO_2 generated on-site and increase H_2 yields [29]. The effectiveness of calcium oxide as an in-bed catalyst for reforming or cracking tars produced by thermally degrading hydrocarbon fuels has long been known [30]. CaO materials have Lewis basic (O^{2-}) and acidic (Ca^{2+}) sites. The substantial might have the right acidity-basicity equilibrium to catalyze the reaction, more precisely, the in-situ pyrolysis-catalytic steam reforming reaction of PS dissolved in phenol. CaO has drawbacks, including poor long-term stability and a high-temperature regeneration need. As a result, efforts have been made to increase this element's endurance by adding a second metal oxide to the CaO using the synergy between the metals to increase coke resistance and active phase dispersion. Due to its affordability, relative stability, and ability to provide a variety of surface areas and porosities through its many phases, alumina is frequently utilized as a catalyst carrier [31]. Alumina's surface possesses acidity and hydroxyl group functionality, which may have strong metal-support interactions (SMSI) [32,33].

This study synthesized transition and noble metal-free catalysts from alpha alumina and calcium oxide to cogenerate H_2 and liquid fuel from pyrolysis catalytic steam reforming reaction of PS waste dissolved in phenol. We changed the experimental setup and attached a Parr Benchtop Reactor (PBR) to boost the ratio of PS to phenol to 2:8, which is significantly greater than our earlier efforts [20,34,35] (see Fig. 2). With this adjustment, more polymer and plastic debris may be added to the reaction without clogging the lines, and it is much easier to liquefy. Thus, the novelty of this research falls into the facile synthesis of transition and noble metal-free catalysts, cogenerate H_2 and liquid fuel, and the reactor design for PS waste recycling with higher ratios and feasibility. Catalysts, namely Ca, 2Ca2Al (Ca:Al volume ratio of 2:2), and 2Ca3Al (Ca:Al volume ratio of 2:3), were synthesized by impregnation and hydrothermal techniques. Fresh samples were analyzed by nitrogen (N_2) adsorption-desorption isotherms, Brunauer-Emmett-Teller (BET) surface area, transmission electron microscopy (TEM), scanning electron microscopy (SEM), energy dispersive X-ray (EDX) element mapping analysis, X-ray powder diffraction (XRD), fourier-transform infrared spectroscopy-potassium bromide (FTIR-KBr), temperature-programmed desorption of ammonia (NH_3-TPD), X-ray photoelectron spectroscopy (XPS) spectra, temperature programmed desorption of carbon dioxide (CO_2-TPD), pyrrole-differential thermogravimetric analysis (DTG) and thermogravimetric analysis (TGA) curves, pyrrole-FTIR spectra, pyridine FTIR spectra, and pyridine TGA-DTG analysis, H_2 temperature-programmed reduction (H_2-TPR). The gas products were examined by gas chromatography using a thermal conductivity detector (GC-TCD), and liquid products were analyzed by gas chromatography/mass spectrometry (GC/MS), gas chromatography using a flame ionization detection (GC-FID), and FTIR systems. Spent samples were also examined by the elemental analyzer (carbon, hydrogen, nitrogen, and sulfur (CHNS)), TGA-DTG, FTIR-KBr, N_2 adsorption-desorption isotherms, BET surface area, SEM, EDX, and TEM analysis.

2. Materials and methods

2.1. Preparation of Ca-Al nano-catalysts

The materials were dried in static ambient air at 110 °C for 12 h before use. Nanocatalysts were synthesized using hydrothermal followed by impregnation methods by depositing alumina powder in the calcium oxide. This method was reported in detail in our previous research [34,35], and the preparation procedure is depicted in Fig. 1. Briefly, specific amounts of γ-Al_2O_3 and CaO materials were dissolved in deionized water and gently stirred at room temperature for an hour. Then, nano Al and nano Ca materials were individually synthesized by adding the 6 M sodium hydroxide (NaOH) dropwise to an aqueous solution of γ-Al_2O_3 and CaO. NaOH was employed to improve the

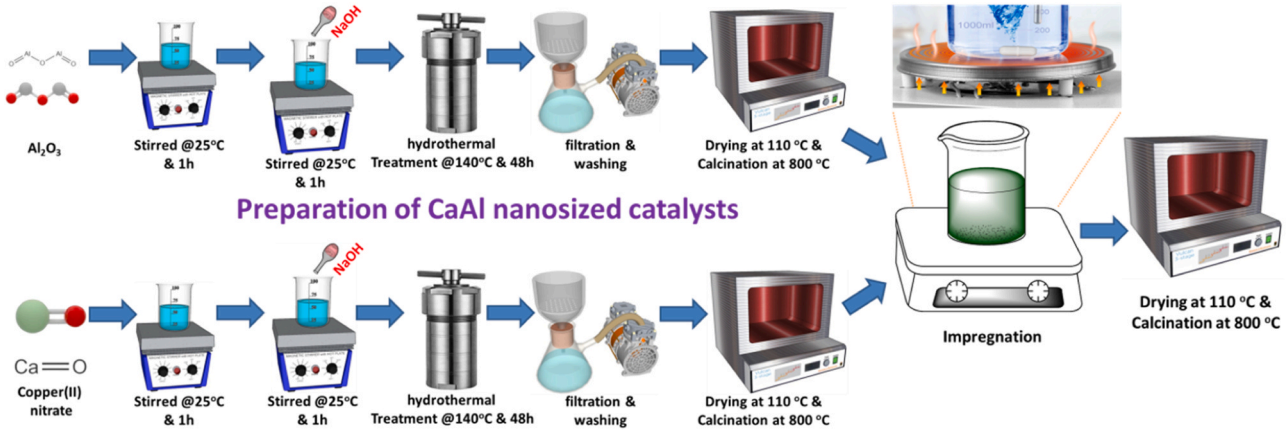

Fig. 1. Synthesis procedure of Ca, 2Ca2Al, and 2Ca3Al nano-sized catalysts.

nucleation and growth rates of the nanoparticles [36] and stirred for one more hour at room temperature. The solutions were heated in an oven at 140 °C for 48 h in a 100 mL Teflon cylinder sealed in a stainless steel autoclave reactor. After cooling the autoclave reactor at room temperature, the produced powder was filtered and repeatedly washed with deionized water, dried at 110 °C overnight, and calcined at 800 °C for 3 h. The filter paper was used in a Buchner funnel placed on top of a sidearm conical flask and sealed with a rubber bung for faster filtering and washing operation. A vacuum pump was attached to the side arm of the flusk to hasten the filtering and washing process. Prepared nanomaterials were then undergone through the impregnation method. Typically, a specific amount of Ca nanomaterial was diluted to 150 mL of deionized water at room temperature and stirred for one hour to form a clear solution. Then, the obtained Al nanoparticles from the hydrothermal method were added dropwise into the Ca mixture under stirring. The obtained suspensions were stirred at 90 °C until most water molecules evaporated and slurry formed. The formed slurry was dried at 110 °C for 12 h in an oven (model: Ney Vulcan D-130). Finally, the samples were calcined at 800 °C for 3 h and sieved on two layers of 35 and 34 mesh to acquire the particle sizes between 1.0 mm and 1.4 mm.

2.2. Characterizations

The morphology and structure of Ca, 2Ca2Al, and 2Ca3Al nanocatalysts were characterized by various techniques, including XRD (D8 ADVANCE Bruker diffractometer), TEM (JEOL JEM-1011 microscope operating at 80 kV), SEM and EDX (FEI QUANTA 600), FTIR-KBr (Shimadzu IR-Prestige-21 spectrometer), N_2 adsorption-desorption measurements and BET surface area (kman Coulter SA3100™ instrument). The BET model determined the surface area from the N_2-isotherm data. The reducibility (H_2-TPR) and basicity (CO_2-TPD) investigations of the fresh catalysts were conducted by Micromeritics Chemisorb 2720 apparatus. The acidity (NH_3-TPD) of the fresh samples was analyzed by the Micromeritics AutoChem II 2920 Automated Catalyst Characterization System. Pyrrole TGA further examined the basicity study and DTG (Shimadzu TG-50 equipment), and pyrrole adsorbed FTIR (Shimadzu IR-Prestige-21), and procedures are stated in the previous research [37,38]. Pyridine TGA also investigated the acidity of the fresh catalysts, and DTG (Shimadzu TG-50 equipment) and pyridine adsorbed FTIR (Shimadzu IR-Prestige-21) and following the previous research [39,40].

TGA, DTG, TEM, SEM, EDX, and CHNS elemental analyzers were used to assess the quantity and type of coke production on the spent catalysts following their employment in the in-situ pyrolysis-catalytic steam reforming settings. A JEOL JEM-1011 microscope operating at 80 kV was used to take TEM pictures of the spent catalyst. By sonicating the catalyst powder in acetone and placing it over a thin copper grid coated with carbon, TEM specimens were created. The Shimadzu TG-50 equipment was used to conduct the TGA analysis using a nitrogen flow at a 20 °C/min heating rate.

2.3. Catalyst screening

Fig. 2 shows a general scheme of an in-situ pyrolysis-catalytic steam reforming system. As reported previously [41–43], the catalytic reaction was carried out in a fixed-bed reactor with an inner diameter of 8 mm and a length of 300 mm and placed in a furnace where the temperature is monitored. A K-type thermocouple was placed on the top of the catalyst-bed controlled by an electronic furnace. In this regard, 0.25 g of catalyst in each test was first held by quartz wool employed in the center of the reactor and reduced with pure H_2 flow of 30 mL/min at 600 °C for an hour. Each run was repeated at least six times to confirm accuracy and reproducibility. At the beginning of the reaction, the PS waste particles were dissolved in phenol with a ratio of 2:8 at 70 °C using 100 mL Parr benchtop hydrothermal reactor model 4590 equipped with an overhead stirrer to homogenize the PS and phenol solution before the reaction and pumped into the fixed bed reactor by the pressure of nitrogen. The catalysts were screened under atmospheric pressure conditions, a steam-to-carbon (S/C) ratio of 45, and a space-time of 3.75 s at a temperature of 500 °C. All pipes before the fixed-bed reactor were swathed with quartz-glass insulated heating tape at 200 °C to vaporize the PS-phenol solution and water and further diluted by N_2 internal standard. Water was introduced by a high-performance liquid chromatography (HPLC) pump, preheated and vaporized at 200 °C, and then was transferred to the reactor by a flow containing a mixture of N_2 as a carrier gas. The flow rate of the feed (PS-phenol solution) and water was controlled using two volumetric flow controllers to maintain a ratio of 1:9. The outlet of the fixed bed reactor was connected to a coil glass tube condenser, cooled with a circular water-cooled chiller system at 10 °C, to condense the non-reacted steam and pyrolysis products. The non-condensable gas products were examined online employing a GC-TCD (Agilent 6890 N), and the conversion of liquid product was analyzed using a GC-FID (HP 5890 Series II) equipped with a 0.53 mm x 30 m CP-Wax capillary column and the catalytic pyrolysis products GC/MS (Agilent 7890B). The result analyses, such as feed conversion and produced gas composition in yield, were calculated following our previous research [19] and as shown in Eqs. (1)–(4).

$$feed \quad conversion(\%) = \frac{[feed]_{in} - [feed]_{out}}{[feed]_{in}} \times 100 \tag{1}$$

$$H_2 \quad yield(\%) = \frac{moles \quad of \quad H_2 \quad obtained}{moles \quad of \quad H_2 \quad stoichiometric} \times 100 \tag{2}$$

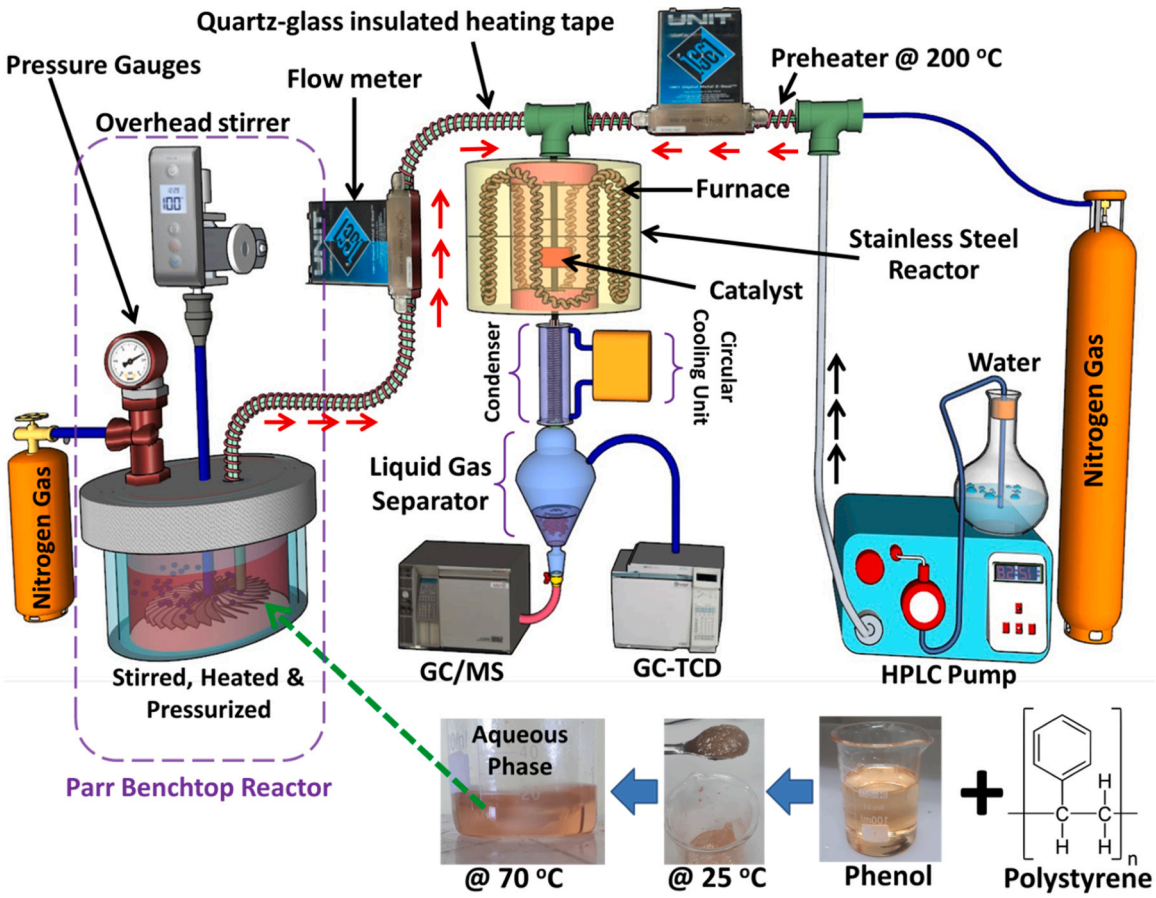

Fig. 2. Diagram of the employed fixed bed reactor system for the in-situ pyrolysis-catalytic steam reforming reaction.

$$CO \quad yield \quad (\%) = \frac{moles \quad of \quad CO \quad obtained}{moles \quad of \quad CO \quad stoichiometric} \times 100 \tag{3}$$

$$CO_2 \quad yield \quad (\%) = \frac{moles \quad of \quad CO_2 \quad obtained}{moles \quad of \quad CO_2 \quad stoichiometric} \times 100 \tag{4}$$

The weight of hydrogen gas in grams per 100 g of feed was determined by applying Eq. (5).

$$H_2 \quad (g) = \frac{Grams \quad of \quad hydrogen \quad gas \quad produced}{Grams \quad of \quad PS-phenol \quad fed} \times 100 \tag{5}$$

The stoichiometric moles are the amount of each chemical that must react for the reaction to be adequately catalyzed. So, for instance, Eq. 6 is the steam reforming equation for balance.

$$C_6H_5OH + 11H_2O \longrightarrow 6CO_2 + 14H_2 \quad \Delta H^o = 463.65 kJ/mol \tag{6}$$

$$C_6H_5OH + 5H_2O \longrightarrow 6CO + 8H_2 \quad \Delta H^o = 710.91 kJ/mol \tag{7}$$

$$CO + H_2O \leftrightarrow CO_2 + H_2 \quad \Delta H^o = -41.15 kJ/mol \tag{8}$$

For instance, we attempted to utilize the following computation to change 10 mL of phenol into stoichiometric moles of H_2. The same procedure can be applied to stoichiometric moles of CO and CO_2.

$$10mL \quad phenol * \frac{1.07g \quad Phenol}{1mL \quad phenol} * \frac{1mole \quad Phenol}{94.11g \quad phenol} * \frac{14mole \quad H_2}{1mole \quad phenol} = 1.59 stochiometric \quad moles \quad of \quad H_2 \tag{9}$$

3. Results and discussion

3.1. Catalyst characterizations

Textural characteristics are the primary factor of catalyst activity in the in-situ pyrolysis-catalytic steam reforming reaction. As a result, XRD experiments of the fresh Ca, 2Ca2Al, and 2Ca3Al nano-sized catalysts were performed. XRD curves to determine the crystal structure and quantitative crystal data are shown in Fig. 3(a) and Table 1, respectively. It is worth emphasizing that the crystal size is denoted by the crystallite thickness, which is determined based on the average size of the crystallites at each diffraction angle of every crystal plane. The X'pert high score plus software was used to analyze the raw data file. All XRD patterns show the reflections of typical cubic spinel structures corresponding to lime materials at 32.2°, 37.4°, 53.9°, 64.2°, 67.4°, 79.7°, and 88.5, that was signed by red stars and correspond to 111, 020, 022, 131, 222, 040, and 133 diffractions with the crystal size of 242.2 nm (JCPDS 96–900–6713), respectively. The diffraction peak at 91.5° (signed with the purple triangle) can be attributed to the 318 crystal phase of rhombohedral $CaCO_3$ (JCPDS 00–005–0586) that almost disappeared after the incorporation of Al_2O_3. The diffraction peaks for oxygen molecules (with blue stars and JCPDS 96–152–8621) were observed at 2θ of 18.4, 29.3, and 62.5, corresponding to the 101, 201, and 421 crystal plane of tetragonal structure with 39.4 nm of crystal size, respectively. The diffraction peaks at 18.1°, 27.9°, 29.8°, 33.5°, 36.8°, 41.3°, 44.1°, 46.7°, 51.8°, 52.9°, 54.1°, 55.3°, 57.6°, 67.2°, and 72.3° (marked with green stars) correspond to the 121, 132, 040, 042, 242, 152, 053, 253, 163, 444, 071, 064, 264, 374, and 284 cubic crystal planes of Mayenite ($Ca_{24}Al_{28}O_{64}$); with 38.9 nm of crystal size (JCPDS 96–901–1411), respectively. These results indicate that Ca-Al alloys were successfully synthesized in the present study. The orthorhombic

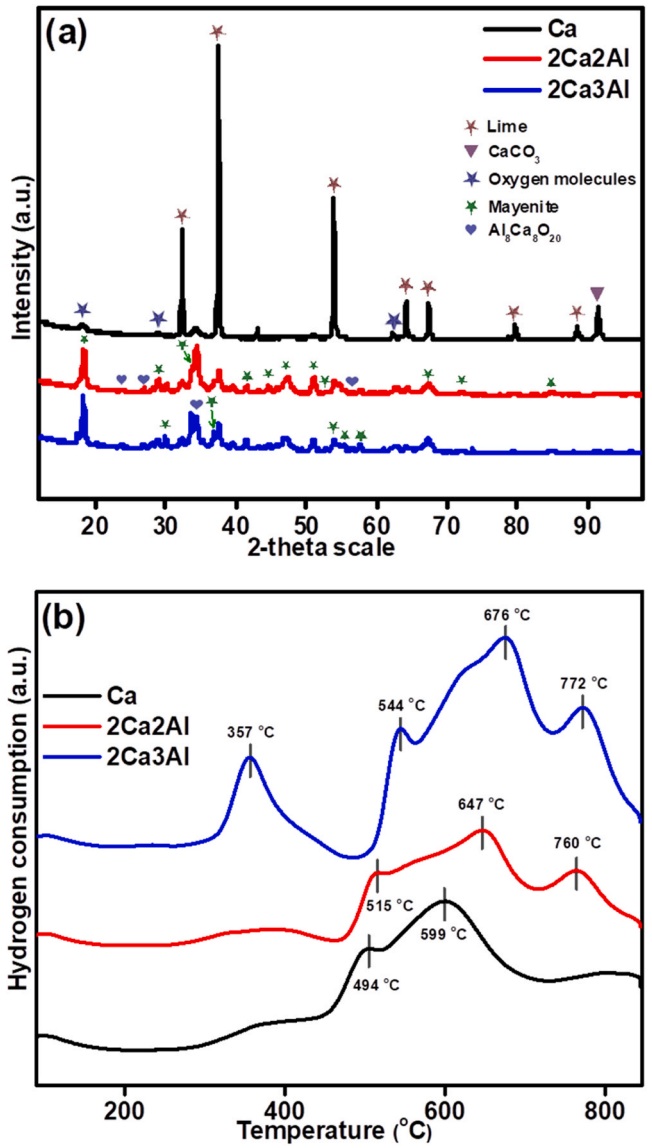

Fig. 3. (a) XRD profile and (b) H_2-TPR curves of the fresh catalysts.

phase structure of $Al_8Ca_8O_{20}$ alloys with 37.7 nm of crystal size (marked with blue hearts) was also confirmed by characteristic peaks at around 23.7°, 26.7°, 34.4°, and 56.4° agreeing with 011, 211, 411, and 811 crystal planes (JCPDS 96–900–2390), respectively. The formation of $Ca_{24}Al_{28}O_{64}$ and $Al_8Ca_8O_{20}$ alloys proves the strong interaction between γ-Al_2O_3 and CaO nanoparticles (SMSI). However, these peaks appeared weak for this crystal plane, suggesting only a few alumina layers stacking in the calcium nanoparticles. The crystal peaks' intensities were reduced at 32.2°, 37.4°, and 53.9° for 2Ca2Al and 2Ca3Al, mainly due to removing some Ca atoms after Al nanoparticles impregnation, hence decreasing the crystal. After introducing the alumina materials, it can be seen that the average crystal sizes estimated by the Scherrer equation were improved by reducing from 61.2 nm to 15.07 nm and 15.94 nm.

We also carried out the H_2-TPR investigation for the fresh catalysts to learn more about the impact of support materials, pre-treatment techniques, and the effects of metal additions on the catalyst reducibility. The results are illustrated in Fig. 3(b) and Table 1. This procedure is crucial to investigating catalysts because it offers precise information on the reducibility of catalysts and reaction rates in the presence of metal surfaces. TPR analysis aids in concluding the reproducibility of catalysts, and supports the quality control of currently used catalytic substances by establishing standards or reduction profiles that ideal manufactured catalysts should follow. For the Ca sample, the peak seen at about 600 °C was connected to the process of $CaCO_3$'s breakdown, which is brought about by CaO carbonation [44]. Furthermore, CaO materials, atmospheric carbon dioxide, and humidity in the air can react at room temperature to generate amorphous $CaCO_3$ on the surface of the particles [45,46]. This is coherent with the XRD results of the calcined Ca catalyst. Additionally, the strong Ca-O bond made it challenging to reduce bulk CaO. However, a minor reduction peak (215.7 **μ**mol.g^{-1}) at a high temperature (559 °C) was presumably brought on by a small amount of surface-based Ca–O bond reduction. In contrast, the broad reduction peak in the 650–770 °C is attributed to the reducibility of stronger Ca species interacting with the Al nanomaterials. The H_2 consumption increased to 407.4 **μ**mol.g^{-1} and 834.5 **μ**mol.g^{-1} for 2Ca2Al and 2Ca3Al nanocatalysts, respectively. This behavior indicated that incorporating Al_2O_3 into CaO materials promoted the reduction of the catalyst. The reduction peak observed at 357 °C is likely associated with reducing the active phase species of CaO, given that the Al_2O_3 materials remain unreduced from ambient temperature up to 500 °C [47]. The significant coverage of CaO on the catalyst's surface caused the reducibility curve for the 2Ca3Al nanocatalyst to shift slightly to a higher temperature. Thus, the higher Al_2O_3 content in the catalyst could affect its catalytic performance within an ideal range.

The SEM and EDX analysis of morphology and element percentage composition data are shown in Fig. 4. The structure images of the 2Ca3Al nanocatalyst are shown as relatively spherical with a rough surface. The homogeneous distribution of Ca, Al, and O, with an abundance of Ca and O over 2Ca3Al nanocatalyst, was approved by energy-dispersive X-ray spectroscopic (EDX) elemental mappings. The content of Ca was higher than Al, while the signal of Ca and O in the mapping image was stronger than that for Al, indicating that Ca was distributed on the outer layer of the body of the catalyst and due to the Ca-rich mayenite structure as proved by XRD analysis. The spectrum also shows the peak for Al, Ca, and O, indicating the formation of Ca-Al-O alloys on the surface of the 2Ca3Al sample, which agrees with the XRD analysis (see Fig. 3(a)). The spectrum peaks show that there is less percentage of Al compound found on the surface of the 2Ca3Al nanocatalyst. The low rate of alumina might be due to the low beam voltages, which weaken the edge influences and increase surface topographic information in the pictures. Another reason behind this low percentage might be the small particle sizes of Al and because the Ca nanoparticles act as inhibitor molecules which causes the reduction of the detecting of Al particles. This becomes difficult at very high magnifications, like in the case of nanoparticles with diameters far below 100 nm. The morphology of the 2Ca3Al was further examined by TEM (see Fig. 5).

The maximum magnification available in the area of microscopy is provided by TEM, which may reveal details on surface characteristics, shape, size, and structure. The TEM results of the 2Ca3Al nanocatalyst are shown in Fig. 5, indicating that Al nanoparticles were uniformly

Table 1
BET surface area, pore diameter, pore-volume, reducibility, basicity, and crystal sizes record the fresh nanocatalysts.

Catalyst	Crystal size (nm)	Surface area ($m^2.g^{-1}$)	Pore-volume ($cm^3.g^{-1}$)	Pore-diameter (nm)	CO_2 uptake (μmol.g^{-1})	H_2-Consumption (μmol.g^{-1})
Ca	61.16	13.76	0.091	26.59	164.8	215.7
2Ca2Al	15.07	64.59	0.235	14.55	220.3	407.4
2Ca3Al	15.94	72.39	0.267	14.74	265.5	834.5

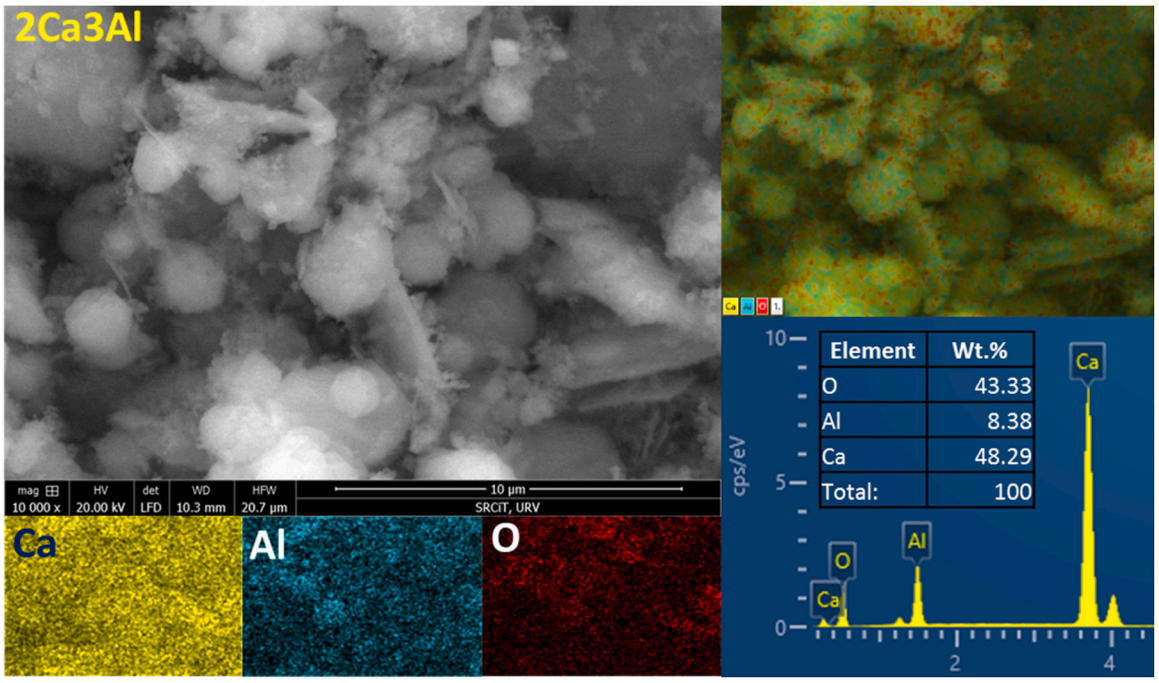

Fig. 4. SEM, EDX, and Elemental mapping analysis of as prepared 2Ca3Al nanocatalyst.

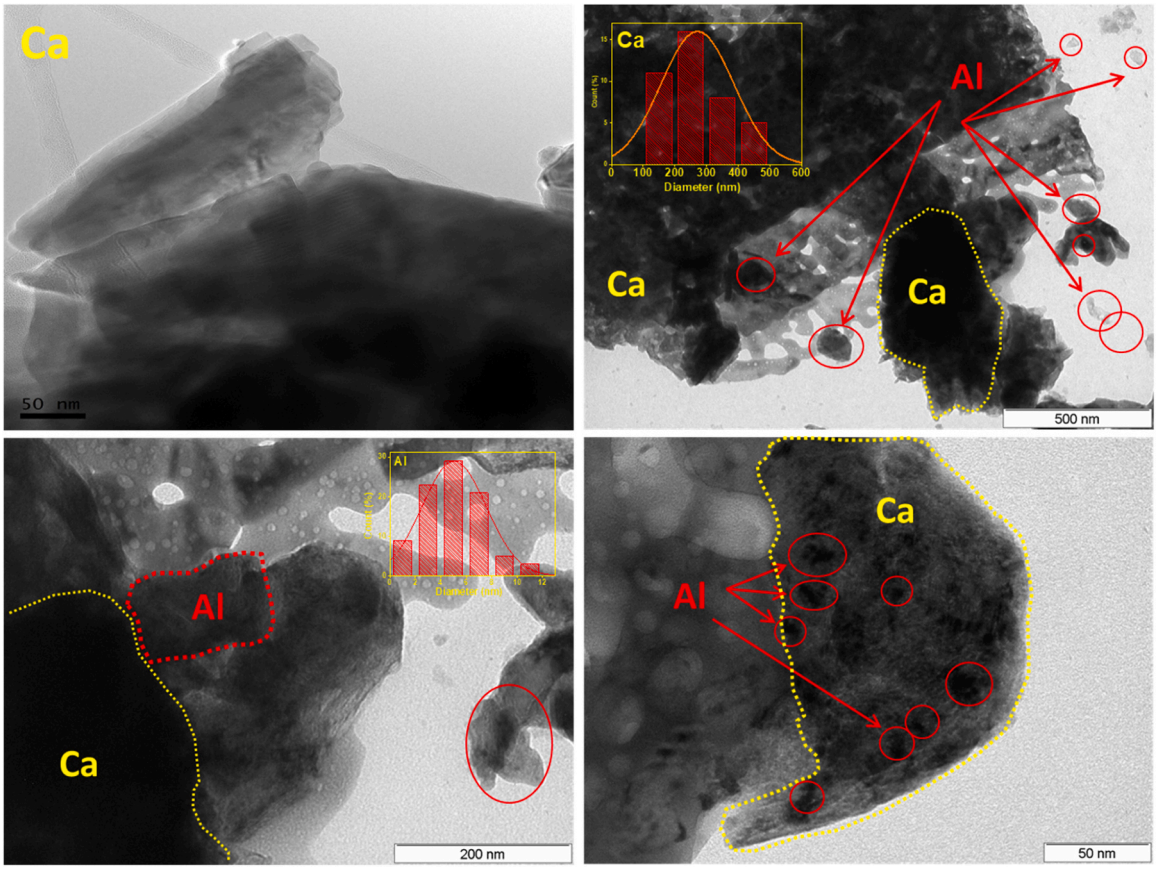

Fig. 5. TEM illustrations of the fresh Ca and 2Ca3Al nanocatalyst and its corresponding size distribution histograms.

distributed and loading on the Ca nanoparticles with plenty of holes on the surface. The thicker crystal wall of the Ca nano materials prevents the TEM from penetrating it, resulting in a dark region in the middle of the composites. Many distinct, consistent, and easily observable microporous structures were present on the surface of Ca, which was relatively smooth and flake-like. The average diameter of the particles was calculated using ImageJ 1.52 v software, while the data was graphically represented through the utilization of the histogram

function of OriginPro software. The average void diameters of the spherical mesoporous Ca hollow spheres are around 10–70 nm. According to the photos, the average diameter of Ca and Al nanoparticles is roughly 270 nm and 5 nm, respectively. These photographs show irregularly shaped particles that exhibit various interactions between the variously sized precursors. Notably, certain particles observed in the TEM images exhibit a significantly larger size than those determined through XRD analysis. This discrepancy can be attributed to the crystal size obtained from XRD measurements indicating the crystalline characteristics. In contrast, the morphological structure of the generated nanoparticle clusters is evident from the TEM images.

The BET surface area, N_2 adsorption-desorption isotherms, and pore size distribution plots are shown in Table 1 and Fig. 6(a and b), respectively. The N_2 adsorption/desorption isotherm is exhibited in Fig. 6, where the volume of adsorbate (N_2) adsorbed on the surface of adsorbent (catalyst) at standard temperature and pressure (STP) was drawn alongside relative pressure of P/Po (the pressure at equilibrium over saturation pressure of adsorbates) at a constant temperature. The capillary condensation of the adsorbate causes the presentation of a hysteresis loop in adsorption isotherms. Following the International Union of Pure and Applied Chemistry (IUPAC) classification [48,49], the N_2 adsorption-desorption isotherm shows that Ca catalysts display a type H3 hysteresis loop and 2Ca2Al, and 2Ca3Al samples display most similar to type IV isotherm, suggesting a mesoporous structure. Adsorbate condensation in open slit-shaped capillaries or capillary gaps between parallel plates is thought to cause type-H3 loops. The equivalent pore size distribution (Fig. 6(b)) displays that 2Ca3Al had a narrow peak concentrated at ~8 nm and a broad peak scattering from 20 to 30 nm, signifying that all catalysts comprised a hierarchical porous system containing mesopores. The Ca nanoparticles exhibited a low specific surface area (13.76 $m^2.g^{-1}$) and small pore volume (0.091 $cm^3.g^{-1}$), ascribed to the compact nonporous structure of the bare calcium oxide. In particular, the volume of mesopores with a size of about 5–20 nm was significantly increased due to forming a small multichannel in the 2Ca3Al. These elongated pores with narrow diameters (~8 nm) facilitate the Knudsen diffusion of gas molecules. It is a type of diffusion that occurs when a system's scale length is equal to or less than the mean free path of the particles implicated. Specifically, in tiny channels, the target gases collide more frequently with the channel walls than they do with one another, which causes an efficient reaction with the sensing material in the 2Ca3Al system. Impregnating γ-Al_2O_3 on the CaO significantly increased the BET surface area and pore volumes to 64.59 $m^2.g^{-1}$ and 0.235 $cm^3.g^{-1}$ for the 2Ca2Al and 72.39 $m^2.g^{-1}$ and 0.267 $cm^3.g^{-1}$ for the 2Ca3Al nanocatalyst, respectively, as γ-Al_2O_3 is well known for its high porosity. This is because the walls of this hollow sample would retain more mesopores as the amount of Ca nanoparticles decreased. It is important to note that while the presence of these newly formed mesopores may enhance mass transfer in catalysis, they may also alter the catalytic performance and stability of the in-situ pyrolysis-catalytic steam reforming reaction if they expose more accessible active edge sites of Ca-Al alloys.

A molecule's basicity is determined by how well it can receive a proton (H^+) and produce a stable end product. In this regard, we analyzed the fresh catalysts by CO_2-TPD, pyrrole-adsorbed TGA-DTG, and pyrrole-adsorbed FTIR spectra, and the findings are displayed in Fig. 7(a, b, and c). In general, CO_2 has advantages that can penetrate all pores of solid catalysts owing to its small molecule size. Pyrrole is an amphoteric molecule that may function as a proton acceptor through its π electron orbital or a proton donor to interact with basic sites on the surface. The pyrrole ring contact with the metal cation drives the pyrrole interaction with the metal cation (Lewis acid site), and the pyrrole NH group's hydrogen connection with the oxygen atom of the framework further stabilizes it. The curves in Fig. 7(a) can be classified into weak (<200 °C, in yellow), medium (200–600 °C, in purple), and strong basicity (>600 °C, in pink) regions, ascribed to a surface hydroxyl group (-OH), surface oxygen anion and bulk oxygen anion/oxygen vacancy sites, respectively. The medium and strong basic sites were generated by the chemisorption of CO_2 on both the outer surface, which consists of the $Ca(OH)_2$ phase, and the bulk region of the CaO nanoparticles [50,51]. A shoulder desorption peak at ~260 °C appears for the 2Ca3Al nanocatalyst, suggesting the creation of new chemisorbed phases, which are likely the ionic oxygen classes initiating from the lattice of γ-Al_2O_3. CO_2 molecules can adsorb on the support or the phases traced close to the γ-Al_2O_3-CaO interface region by developing suitable carbonyl, hydroxycarbonate, or carbonate groups. The figure indicates that introducing γ-Al_2O_3 does not induce any modifications in the strong basic site, as all samples exhibit comparable desorption peaks in that region. This outcome may be attributed to the desorption bands' tendency to react with CO_2 pre-adsorbed on the CaO surface, forming lime. Higher desorption temperatures specify a strong interaction among γ-Al_2O_3 and CaO nanoparticles, as previously described in XRD and H_2-TPR analysis (see Fig. 3). Compared to the bare Ca nanocatalyst (164.8 μmol.g-1), the CO_2 uptake densities of 2Ca2Al and 2Ca3Al increase significantly to 220.3 μmol.g^{-1} and 265.5 μmol.g^{-1}, respectively, due to increased surface oxygen vacancy density. It can be observed that the chemical adsorption of CO_2 is slightly stronger for the 2Ca3Al catalyst compared

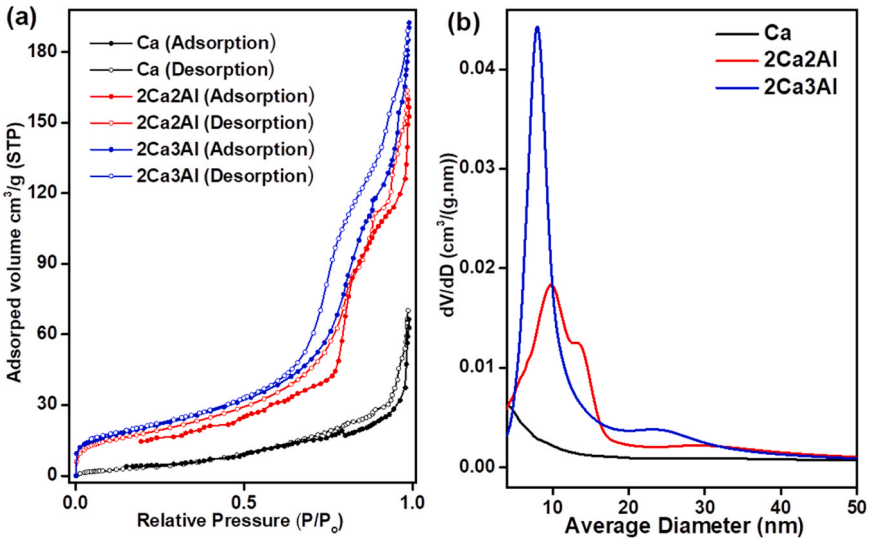

Fig. 6. (a) N_2 adsorption-desorption isotherms and (b) pore size distribution plots of the fresh catalysts.

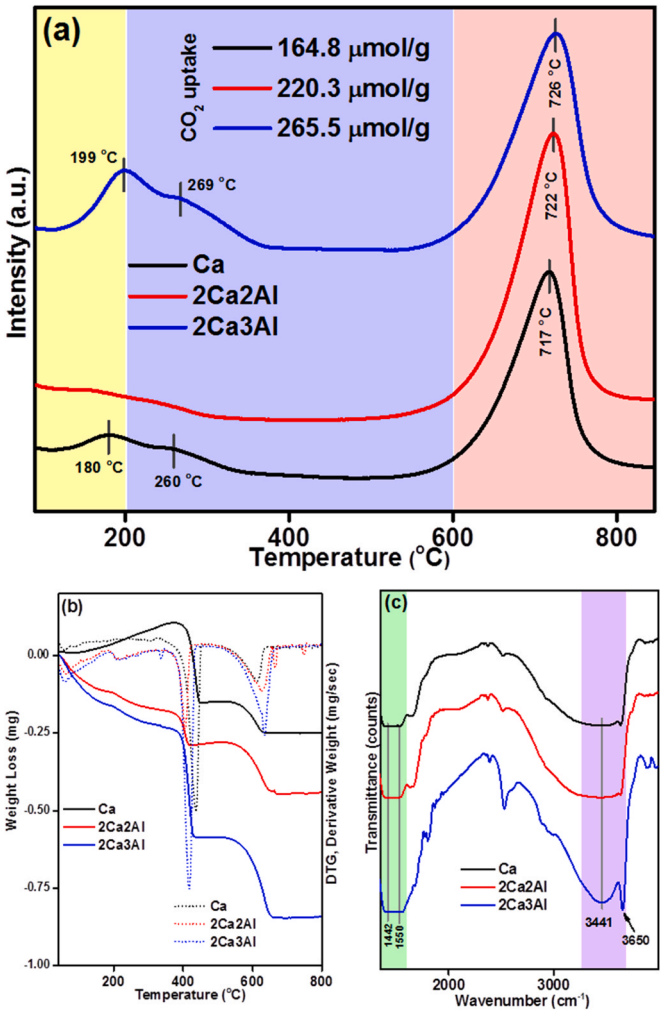

Fig. 7. (a) CO_2-TPD curves, (b) pyrrole TGA and DTG curves, and (c) pyrrole adsorbed FTIR spectra curves of the fresh catalysts.

to the 2Ca2Al and Ca catalysts. The pyrrole TGA-DTG profile (Fig. 7(b)) showed how the peak intensities seen at ~ 400 °C reflect the pattern of the pyrrole-FTIR (Fig. 7(c)) and CO_2-TPD (Fig. 7(a)) spectra (2Ca3Al>2Ca2Al>Ca). The two successive carbon atoms in the cycle form an adsorption layer on the Bronsted sites, which has far lower adsorption energies than the Lewis sites. It is suggested that the higher amount of γ-Al_2O_3 provides more convenience for CO_2 adsorption and activation, which is the key to high catalytic performance in the in-situ pyrolysis-catalytic steam reforming reaction of PS dissolved in phenol.

Pyrrole (C_4H_4NH) was utilized to test the strength of the catalyst's basic sites in the NH–O absorption band v(NH) through the atomic molecule H. The finding of basic sites traced at the catalyst surface and the amount of the basicity strength were also perceived by the N−H stretching peaks at 3650–3250 cm^{-1} by using pyrrole probed FTIR spectroscopy (Fig. 7(c)); whereas the N–H strip (liquid-like physisorbed pyrrole) comes into interaction with the π-system of the adjacent pyrrole particles. The 2Ca3Al nanocatalyst has a sharp transmittant band at 3650 cm^{-1} because of the bending vibration of the hydroxyl (–OH) group at the outer surface of the catalyst. Meanwhile, the peaks at 3650 cm^{-1} corresponding to Ca and 2Ca2Al were significantly reduced, almost disappearing, suggesting a weaker interaction between the catalyst and pyrrole particles than 2Ca3Al. The bands of 2Ca3Al exhibited higher density than those of 2Ca2Al and Ca nanocatalysts. This is noticeable in higher interactions of all pyrrole and pyrrolate classes due to elevated basicity by additional γ-Al_2O_3 nanoparticles in the 2Ca3Al nanocatalyst. According to results, basic sites boost acidic CO_2 activation on the catalyst's surface and prevent carbon from depositing, improving catalytic stability. The broad characteristic FTIR peaks at 1442 cm^{-1} and 1550 cm^{-1} represent the coexistent Lewis and Brønsted basic sites, respectively. This finding may help to explain why the more considerable contribution of Lewis and Brønsted basic sites is linked to the rise in basicity measured by CO_2-TPD with higher γ-Al_2O_3 nanoparticles. According to general agreement, Lewis and Brønsted basic sites are generated as basic sites after the calcination step and correspond to oxygen cations and anions with weak coordination. Pyrrole can bind to catalysts in its H^+ form and components in its alkali cation form, indicating that it can interact with both Lewis acidic sites and Brønsted acidic sites. However, only the framework oxygen atoms can do so at basic sites [52]. As a result, we investigated the pyridine-FTIR and pyridine TGA-DTG for the acidity analysis in more detail (see Fig. 8(a) and (b)).

It is essential to examine the catalyst acidity since it is well known that it favors unintended breakdown and polymerization processes in reforming, producing more coke and less H_2 yield [53,54]. The TGA-DTG technique was used to analyze the catalysts with pyridine adsorption to investigate the coverage of pyridine adsorption on acid sites. The results, presented in Fig. 8(a), depict the relationship between the temperature and the adsorption coverage. The spectra of pyridine coordinately bound to the surface are significantly different compared to the pyridinium ion's spectra. As a result, acid types may be distinguished on the surface of acidic substances [55]. The TGA analysis revealed the changes in physical and chemical properties of Ca, 2Ca2Al, and 2Ca3Al as a function of increasing temperature. Removing physically adsorbed solvent from the catalyst's surface was identified as the cause of a first weight loss of up to 110 °C. It might be attributed to an endothermic process affecting water vapor discharge. The significant weight loss was in the second degradation step at 400–800 °C. DTA additionally supported the TGA. The DTA curve showed two prominent endothermic peaks at 400 °C and 650 °C. The first peak is an endothermic reaction that affects the breakdown of pyridine, whereas the second peak may be caused by the breakdown of the organic component on the catalyst's surface. The acidity constants of these pyridine TDG peaks increased in the following Ca> 2Ca2Al> 2Ca3Al, illustrating the higher acidity belonging to the bare Ca nanocatalyst. A low-acidity catalyst was produced by treating the Ca catalysts with an excess of γ-Al_2O_3 nanoparticles. The significant hydrated γ-Al_2O_3 ion first covered several sites, but after calcination and removal of the hydration water, these sites became more exposed and active.

Fig. 8(b) shows that the pyridine adsorption FTIR spectrum approach was used to qualitatively assess the catalysts' acidity. Pyridine is an appropriate basic probe molecule to evaluate both Brönsted and Lewis acidic sites by FTIR spectroscopy. The peak at wavenumber 1440 cm^{-1} indicated that all of the catalysts' pyridine adsorbed simultaneously on Lewis acid. In contrast, the band about 1550 cm^{-1} was linked to the adsorption of pyridinium ions on Brönsted acidic sites. The adsorption bands appeared between 1440 cm^{-1} and 1550 cm^{-1} due to the adsorbed pyridine on both types of acidity [56]. Incorporating γ-Al_2O_3 into the CaO has caused a significant decrease in Brönsted and Lewis acid sites. A similar observation of the 3641 cm^{-1} and 2515 cm^{-1} band characteristics was perceived for the acid site of the Ca−OH−Al group and C–H stretching in and –CH_2–, respectively. The 2515 cm^{-1} peaks could also be attributed to the Pyridine–H^+ species on the catalyst. The acidity trends of all catalysts followed the TGA-DTG curves (Fig. 8(a)) and decreased in the following Ca> 2Ca2Al> 2Ca3Al, illustrating the higher acidity belonging to the bare Ca nanocatalyst. This result was probably due to the acidity of the catalysts being disturbed by γ-Al_2O_3 nanoparticles. The coverage of γ-Al_2O_3 on the stable Brönsted acid sites probably affected the reduction in the Brönsted and Lewis acid phases. Significantly, the thermal cracking efficiency can be suggestively affected by the quantity and strength spreading of the surface acidity. The cracking process benefits more from acid sites with increasing strength and quantity. However, weakening the Brönsted and Lewis acid

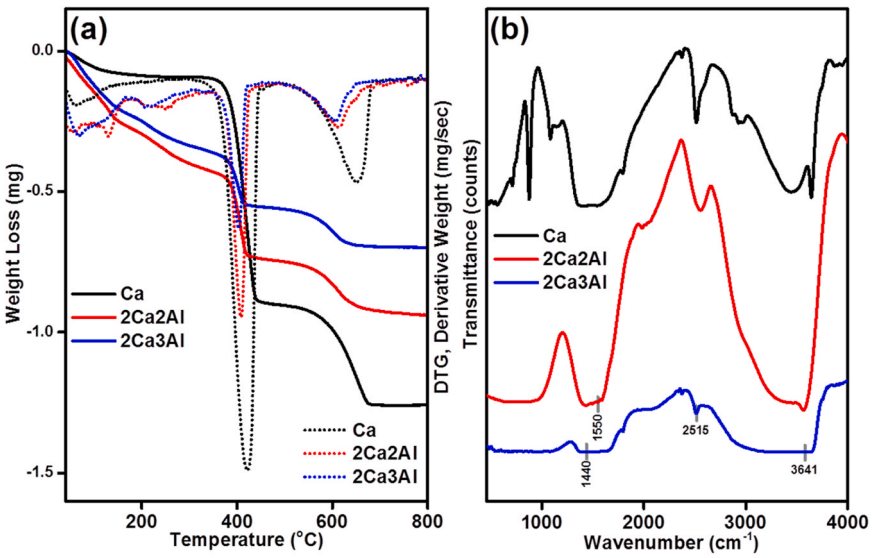

Fig. 8. (a) Pyridine TGA and DTG curves, and (b) pyridine adsorbed FTIR spectra curves of the fresh catalysts.

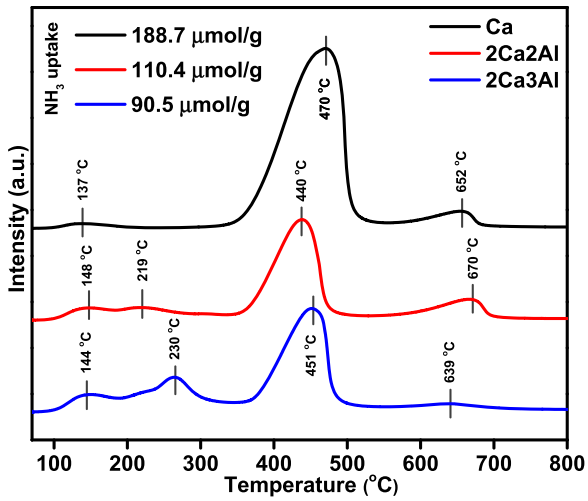

Fig. 9. Temperature-programmed desorption of ammonia (NH_3-TPD) curves of the fresh catalysts.

phases is necessary to stop the undesirable reaction and coke deposition, particularly for the heat breaking of polymer molecules. As a result, it is anticipated that 2Ca3Al would exhibit strong catalytic performance and stability during the in-situ catalytic steam reforming of phenol in conjunction with the pyrolysis of PS waste.

NH_3-TPD analysis was carried out on different samples to check the surface acidity as a function of Al content. NH_3-TPD temperature-programmed desorption profiles of Ca, 2Ca2Al and 2Ca3Al are shown in Fig. 7. Several peaks are appeared in all samples which indicate the presence of different types of acidic sites. In terms of Ca, strong peak at around 470 °C was detected, along with small peaks at 137 °C and also 652 °C. 2Ca2Al exhibits a main peak at 440 °C, and three small peaks at 148, 219 and 652 °C. 2Ca3Al sample shows three peaks with different intensity. The main peak is found at 451 °C, while two peaks are detected at 144 and 230 °C. NH_3-TPD peaks at above 400 °C reflect a stronger acidity of the surface, which in turn boosts C–C and CO– binding unlocking. However, very high acidity may lead to fast surface catalyst deactivation as a result of coke formation [57]. A tradeoff between strong acidity and slow surface deactivation should be obtained to allow the continuously of the process at large scale application. Al based materials exhibit usually Brønsted acidic sites connected by bridging hydroxyl groups, wherein the H^+ species compensate the negative charged sites [58]. In general, this sites are responsible behind for the binding of basic species, i.e., ammonia, by hydrogen bond. On the other hand, Lewis acid sites can be formed by Al with low coordination which can catalyze many important reactions as electron receiver, suggesting enhanced charge transfer. These acidic sites are very important for cracking processes. As compared to bare Ca, both 2Ca2Al and 2Ca3Al samples exhibit softer acidity, however, the main peak in 2Ca3Al shifted a bit to higher acidity because of the involving of more Brønsted acidic sites due to the higher Al content. Also, peaks below 400 °C are more intense in 2Ca3Al as compared to those in 2Ca2Al. Overall, the combination of Ca and Al with optimized content could control the acidity of the catalyst in order to obtain the highest activity along with slow surface deactivation.

Functional groups of the fresh catalysts were analyzed by FTIR-KBr and results are shown in Fig. 10. The transmittant band at 841 cm^{-1} corresponds to CH_2 rocking vibration [59]. This band can also be designated to the O–O the vibration of surface peroxo classes [60]. A similar band was detected for peroxo species bound to zirconia-based oxo groups [61,62]. The intensity of this peak increases with the increasing γ-Al_2O_3, which the forced dissociation of γ-Al_2O_3 can account for into peroxo species that are next captured on the CaO surface (see

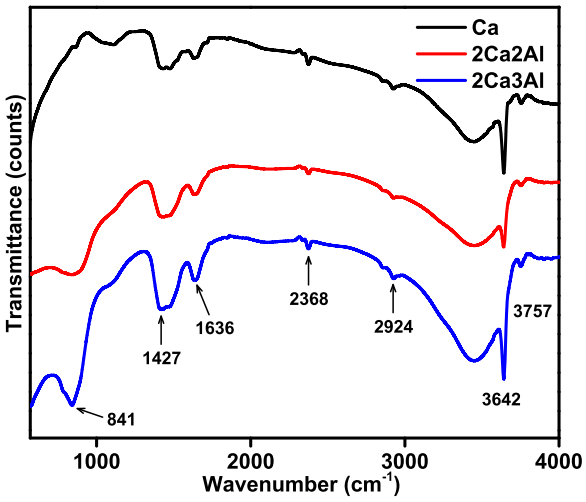

Fig. 10. Fourier transform infrared (FTIR-KBr) profiles of the fresh catalysts.

discussion below). The stronger band found at 1427 cm^{-1} might be ascribed to the representative bending of the –C–H cluster [63]. The peaks located at 2924 cm^{-1} show the symmetric stretching vibrations of C-H in CH_2 groups [64]. The –C–H functionalization provides a new tactical method for synthesizing complicated compounds. The site selectivity of catalyst-controlled –C–H functionalization would not depend on the substrates' innate reactivity, making it an appealing choice. A toolbox of catalysts with each component capable of complexing a different –C–H bond in a particular substrate would be ideal [65]. The stretching vibration peaks of the OCO (ν_{as}(OCO)) carbonyl group were observed at 1636 cm^{-1} [66,67]. The purpose of the carbonyl group is to destabilize the bonds within the carbon chain functionally. The electronegative oxygen atom draws in more electrons than its bound carbon in the carbonyl group. The transmittance bands at 2368 cm^{-1} are linked to the polarizations of the C═O stretching mode of introduced CO_2 molecules [68]. These peaks represent the physical adsorption of CO_2 molecules onto the synthesized samples' surfaces [69]. FTIR characteristic band at regions 3642 cm^{-1} is ascribed to the O–H stretching vibration of the Al–OH and Ca–OH surface hydroxyl groups because some of –OH might be utilized as Brønsted acid sites by providing hydrogen to ammonia [70]. The calcined samples exhibited weak peaks at 3757 cm^{-1}, which can be attributed to terminal hydroxyl groups on the catalysts.

To examine the element proportion and chemical state of the catalysts before reaction, X-ray photoelectron spectroscopy (XPS) of all samples were investigated and results are shown in Fig. 11. In Ca sample, oxygen spectrum is spitted into two sub-bands, at around 530.34 and 532.18 eV which are associated to lattice oxygen O^{2-} and chemically surface sorbed oxygen, respectively. Ca2p spectrum in Ca sample is spitted into two bands at 347.89 and 351.39 eV corresponding to $Ca2p_{3/2}$ and $Ca2p_{1/2}$, respectively. In Ca sample, the peak related to Al element was not appeared. In terms of 2Ca2Al, the peak at 530.41 eV, due to lattice oxygen O^{2-}, was reduced compared to Ca sample. In terms of 2Ca3Al, the peak intensity of oxygen chemical surface sorbed at 532.40 eV was reduced. This change in the intensity is due to the insertion of Al element which changes the structure and surface interactions. A single peak related to Al element at 75.67 and 76.55 eV was observed in 2Ca2Al and 2Ca3Al, respectively. The shift of around 0.88 eV was accounted when the content of Al was increased from 2Al to 3Al in CaAl samples, which corresponds to shift in Ca spectra as well. The shift is due to chemicall interactions between Ca and Al, to chemically form CaAl composite.

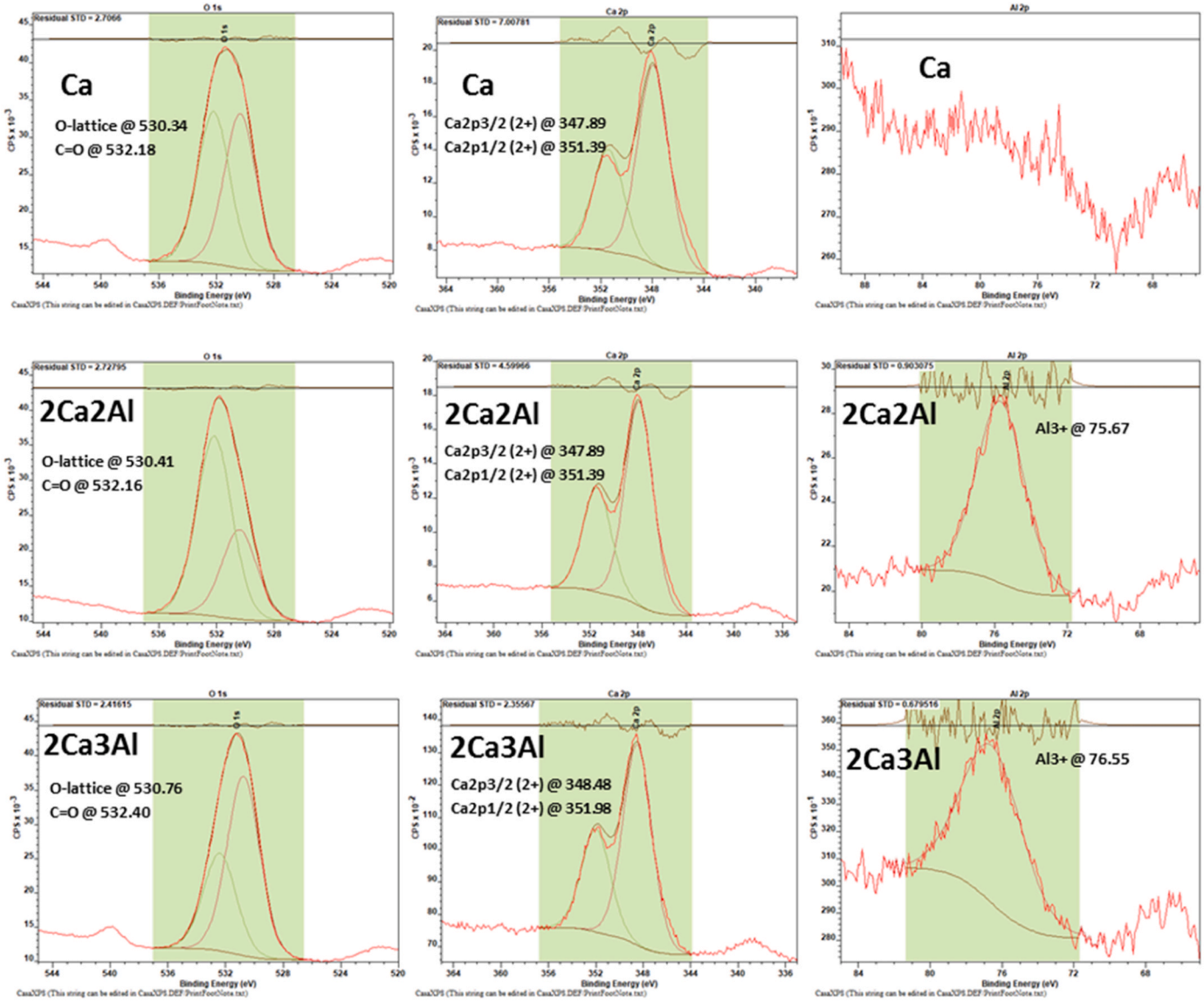

Fig. 11. The XPS spectrum of the fresh catalysts.

3.2. Catalytic performance

Catalysts must be evaluated for activity and selectivity for the intended reaction after being prepared and characterized. The catalytic tests aim to assess the catalyst activity and gather essential data on catalyst behavior, such as catalyst deactivation, lifespan, etc. For this purpose, the catalytic activities of Ca, 2Ca2Al, and 2Ca3Al nano-sized catalysts in the in-situ pyrolysis-catalytic steam reforming reaction of PS dissolved in phenol at 500 °C oil were evaluated, and results are depicted in Fig. 12. The phenol conversion increased as the γ-Al_2O_3 content in the catalysts increased, going from 67.7 % for the bare Ca nanocatalyst to 86.6 % for the 2Ca3Al nanocatalyst. Upon collection of the liquid samples after reactions and subsequent overnight storage in a controlled environment, it was observed that the water content of the produced liquid samples followed the order of Ca< 2Ca2Al< 2Ca3Al, with Ca and 2Ca2Al exhibiting similar amounts of water. Conversely, the remaining feed (the PS-phenol solution) followed the order of Ca> 2Ca2Al> 2Ca3Al, indicating that a more significant proportion of PS-phenol had been converted to the gaseous product in the case of the 2Ca3Al sample. It also can be observed that the H_2 yield and mole fraction increase from 51.2 % and 61.2–64.5 % and 67.5 % for the Ca and 2Ca3Al nanocatalysts, respectively. Ekaterini and Angeliki [71] investigated the suitability of nickel and noble metal catalysts supported on calcium aluminate for hydrogen production via steam reforming of acetic acid and acetone. The steam reforming of acetic acid using calcium aluminate-supported catalysts with varied Ca/Al ratios (1/2 and 12/7) revealed that both Ni (5 wt %) and noble metal catalysts (0.5 wt % Rh and Ir) exhibited high activity. However, the performance of Ni catalysts supported on 12CaO-7Al_2O_3 was found to be inferior to that of their counterparts supported on CaO-2Al_2O_3, primarily due to the higher surface dispersion of Ni on the latter support. The most efficient catalysts for the steam reforming of acetone, namely 5 % Ni/CaO-2Al_2O_3 and 0.5 % Rh/CaO-2Al_2O_3, exhibited comparable activity over the investigated temperature range, with the Rh catalyst displaying a slightly higher hydrogen yield. It is plausible that their identical performance is attributed to the high degree of acetone conversion on the support, especially at the maximum temperature employed. Moreover, the coke deposits on both catalysts were found to be exceedingly low and similar in magnitude, indicative of the widespread nature of the thermal steam reactions. Young and co-authors [72] prepared the nickel-based structured catalysts supported on the modified calcium aluminate (CA_x) with silicon carbide (SiC) to improve the catalytic performance of steam reforming of methane (SRM). The presence of CA_x was essential in enhancing the carbon deposition resistance while achieving high hydrogen production. Furthermore, it was observed that the Ni catalyst supported on SiC-modified CA_x/Al_2O_3 (NASC) displayed more excellent resistance to coke formation than the other catalysts. However, the weak interaction of the active metal and inadequate metal dispersion led to lower methane conversion and H_2 yield efficiency compared to the NAS and NAC catalysts. In our study, smaller crystal sizes with lower pore diameters have more surface area of active sites on the catalyst's surface than large crystals, as seen in Table 1. The greater surface area of the 2Ca3Al, which allows for quicker particle collision rates, contributes to its increased activity. As a result of having a larger surface area to create active sites, the catalyst with a higher pore volume is more active than one with a lower pore volume. As shown in Fig. 3 by XRD and H_2-TPR analysis, the development of catalytic activity similarly matched with the trajectory of the strength of the strong interaction between γ-Al_2O_3 and CaO nanoparticles (SMSI). SMSI occurs when the metal and support strongly interact, changing the metal particles' size, electronic properties, and surface chemistry. SMSI essentially modified the electronic characteristics of the metals on the partly reduced supports through an electronic action. This interaction can result in the nanoparticles becoming highly dispersed on the catalyst's surface, increasing selectivity and catalytic activity. γ-Al_2O_3 can form SMSI when supported on CaO, resulting in highly scattered CaO species with distinctive electrical characteristics that enhance the catalyst's basicity, promoting its activity in various reactions. SMSI between γ-Al_2O_3 and CaO can also increase the catalyst's thermal stability and resistance to sintering, resulting in longer catalyst lifetimes. Therefore, understanding the effects of SMSI between γ-Al_2O_3 and CaO is crucial for optimizing the catalytic properties of supported metal catalysts in various applications. The explanation for this effect was that the oxygen vacancies in the O–H stretching vibration of the Al–OH and Ca–OH surface hydroxyl groups (as seen in the FTIR analysis of Fig. 10) could coordinate the oxygen atoms in phenol and PS plastic wastes. As a result, the polarized C═O band was quickly attacked by hydrogen adsorbed on the γ-Al_2O_3 and CaO nanoparticles in the vicinity of oxygen vacancies. These outcomes also matched the patterns seen with the basicity of the catalysts used in this investigation. Incorporating γ-Al_2O_3 has been found to enhance the performance of the reverse water-gas shift reaction (RWGS: $CO_2 + H_2 \leftrightarrow CO + H_2O$) by decreasing the yield of CO_2 and increasing the yield of CO. By promoting the polarization of water, causing the dissociation of H_2O to generate a hydroxyl group susceptible to adsorption over the catalyst, which is thought to be a kinetically critical stage in the RWGS process, additional hydrogen is produced [73]. Hence, it can be concluded that γ-Al_2O_3 within the catalyst composition promotes RWGS reaction, probably due to increased surface OH-group concentrations. Additionally, water contact can cause the low-coordination O^{2-} anions to change into an OH group [74]. Strong basic sites develop on the strong basic supports due to many low-coordination O^{2-} anions in the corners and edges [75]. The present study illustrates a straightforward reaction mechanism for the in-situ pyrolysis-catalytic steam reforming reaction of polystyrene (PS) dissolved in phenol, as depicted in Fig. 13. The proposed mechanism suggests that PS-phenol undergoes decomposition to yield carbon dioxide (CO_2), while the aforementioned species reacts with hydroxyl (OH) species, thereby generating hydrogen (H_2) and carbon monoxide (CO). Therefore, based on the information provided, the strong basicity sites of the catalyst have a synergistic effect on catalytic activity. The overall number of acid sites does, in fact, negatively correlate with the catalytic activity. This can be explained by the fact that only the sites that accept a proton from the phenol can function as catalysts. Although it is generally recognized that a large number of strong acid sites encourage unexpected breakdown and polymerization processes in reforming, which results in more coke and a lower H_2 yield, this does not always increase performance [53,54]. Fig. 18 provides evidence for this assertion by showing the outcomes of a TGA analysis of the used catalysts. In conclusion, we demonstrated that both catalyst basicity and reducibility play significant roles in the in-situ

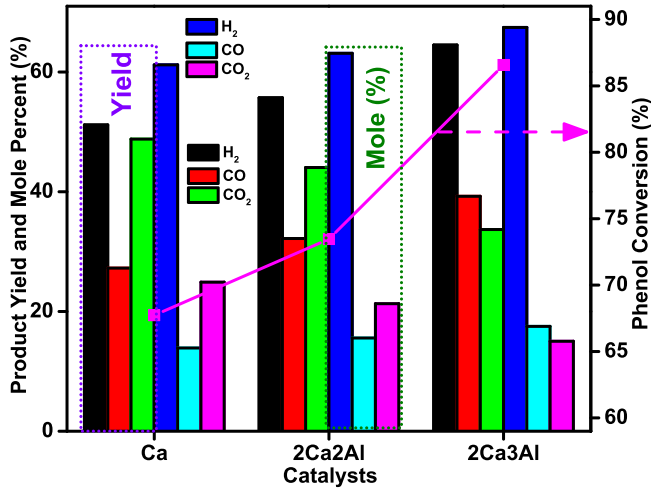

Fig. 12. Reaction performance of the Ca, 2Ca2Al, and 2Ca3Al nano-sized catalysts in the in-situ pyrolysis-catalytic steam reforming reaction of PS dissolved in phenol at 500 °C.

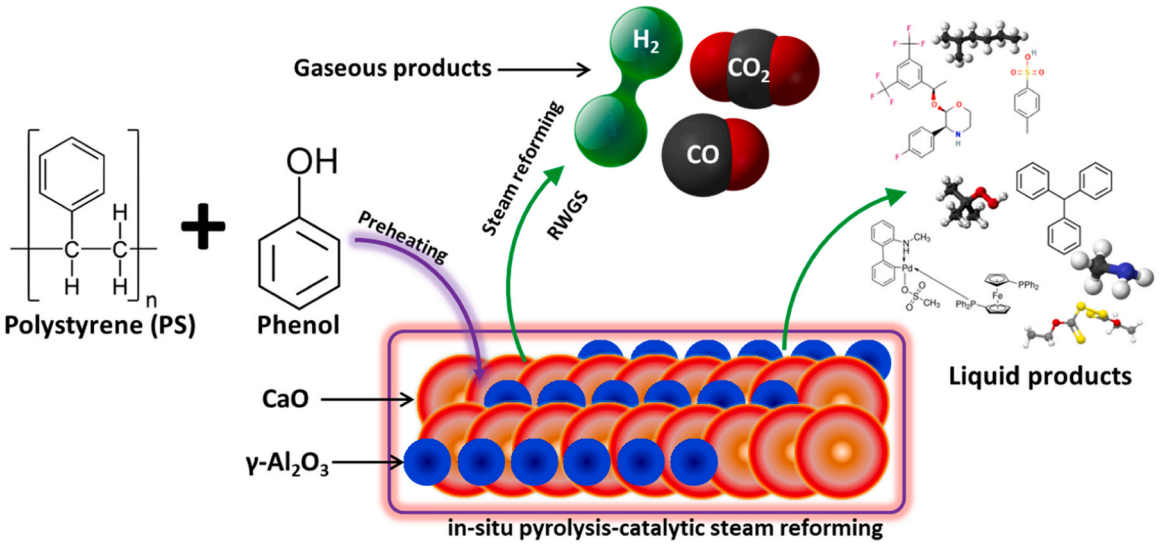

Fig. 13. Functional reaction mechanism for the in-situ pyrolysis-catalytic steam reforming reaction of PS dissolved in phenol.

pyrolysis-catalytic steam reforming reaction of PS dissolved in phenol. Lower and weak acid sites are essential for achieving high catalytic activity in phenol conversion and selectivity towards H_2 production. Considering that the improvement in stability is anticipated given the combination of the chemical and physical properties of the 2Ca3Al nano-catalyst, we examined the impact of temperature and time on stream experiments, as shown in Fig. 14 and Fig. 15, respectively.

Fig. 14 (a) shows the result of the obtained product gas composition for the in-situ pyrolysis-catalytic steam reforming reaction of PS dissolved in phenol at different temperatures. The reaction rate and activation energy were calculated per our previous work [34], and the results are shown in the developed Arrhenius plot in Fig. 14 (b). The quantitative data for grams of hydrogen gas produced per 100 g of feed (PS-phenol solution) are also presented in Fig. 14 (b). The phenol conversion and H_2 yield of the 2Ca3Al nanocatalyst increased with the increase in temperature from 86.6 % and 64.5 % at 500 °C to 98.5 % and 92.5 % at 700 °C, respectively. This increment is due to the endothermic characteristic of phenol steam reforming reaction ($C_6H_5OH + 11H_2O \longrightarrow 6CO_2 + 14H_2$). Because gases have more energy as temperature rises, more colliding particles can pass through the energy barrier (also known as the activation energy (E_a)), which raises the reaction rate ($-r_{ph}$). Consequently, it can be confirmed that the product distribution at 700 °C was much enhanced, and this temperature is the best temperature to produce a high H_2 yield and achieve almost complete phenol conversion. The previous study explores the catalytic steam reforming of acetic acid and phenol for hydrogen production, employing coal ash-supported Ni catalysts as investigated by Shurong and co-authors [76]. The results reveal that at a temperature of 700 °C, acetic acid and phenol conversion rates were considerably enhanced, achieving 98.4 % and 83.5 %, respectively. Furthermore, it has been demonstrated that the performance of the Ni/Ash catalyst was comparable to that of other commercially available Ni-based steam reforming catalysts. Chengxiong et al. [77] used Ni-CaO-$Ca_{12}Al_{14}O_{33}$ catalyst for H_2 production from phenol. In their study, it was asserted that the production of a structure possessing excessive porosity, and the deposition of minute nanoparticles, was facilitated through the in situ creation of carbon templates generated by the adsorption of tetracycline. This approach ensures physical isolation, effectively preventing the sintering of Ca and Ni species. As a result, the catalytic system exhibited consistent and remarkable performance during 50 cyclic tests, with a hydrogen

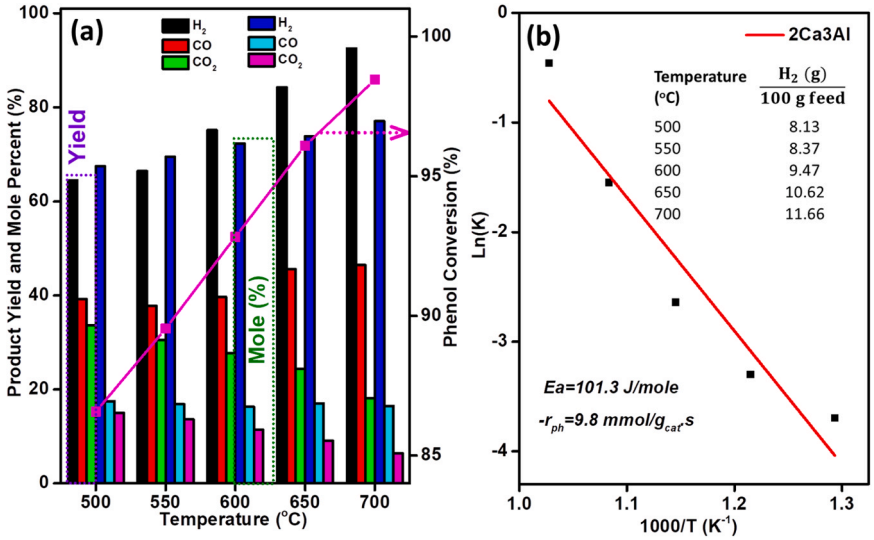

Fig. 14. (a) Phenol conversion, H_2, CO, and CO_2 production as a function of reaction temperature over 2Ca3Al nanocatalyst; (b) Arrhenius plot for PS-phenol steam reforming over the 3Ca2Al nanocatalyst in the temperature range of 500–700 °C.

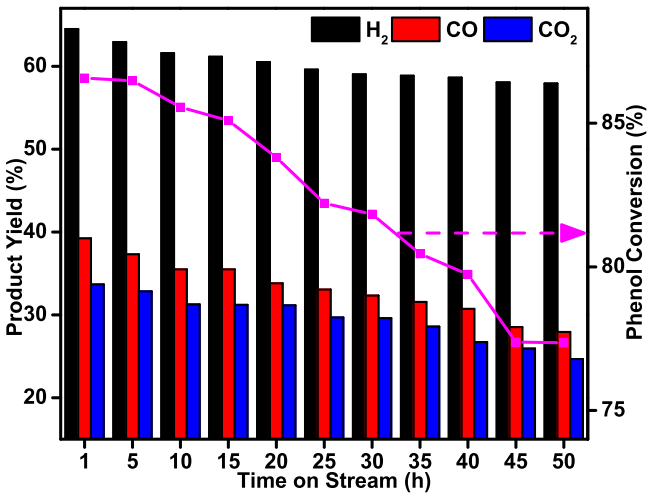

Fig. 15. Stability test over 2Ca3Al nanocatalyst for H_2, CO, and CO_2 production and phenol conversion at 500 °C.

production rate of 98.3 vol % from phenol, and only a 33 % reduction in the sorption-enhancement effect was observed, thus ensuring superior SESR performance of phenol. As seen in Fig. 14 (a), the CO yield increased from 39.2 % at 500 °C to 46.5 % at 700 °C, while the CO_2 yield decreased from 33.7 % to 18.1 % due to the occurrence of the RWGS reaction. Thus, it may be inferred that greater temperatures encourage the RWGS reaction, most likely due to a rise in the concentration of surface OH- groups. The superior performance of the 2Ca3Al nanocatalyst at 700 °C can be attributed primarily to its high efficacy in facilitating the RWGS and steam reforming reactions, as well as its ability to cleave C-C and C-H bonds. Depending on the basic or acidic nature of the catalyst, carbonate, and carboxylate species will accumulate and block the active sites for CO adsorption. It has been discovered that acidic supports are more resistant to CO_2 deactivation than basic sites. When evaluating a possible application, the durability of the catalyst is just as crucial as its activity. This implies that the catalyst should have consistent activity throughout its lifetime or be capable of being quickly renewed to the same level of activity. Thus, clearly defining the stability of novel heterogeneous catalysts is crucial.

Another critical aspect of the deployment of a catalyst is stability. To evaluate the stability of the catalyst against coking and confirm its reversibility under the same reaction conditions, we examined the endurance of the 2Ca3Al nanocatalyst as a function of time on stream at 500 °C for 50 h. The findings are given in Fig. 15. Phenol conversion and H_2 yield decreased with time from 86.6 % and 64.5–79.7 % and 58.6 % after 40 h, respectively. The in-situ pyrolysis-catalytic steam reforming process has a high intrinsic activity; therefore, phenol conversion is not significantly affected even in the presence of coke production or moderate deactivation caused by the aggregation and phase transition of the active phase crystallites. The slight decline in the catalytic activities of the 2Ca3Al nanocatalyst could result from the loss of catalyst deactivation by carbon deposition. However, after over 40 h, no deactivation was observed, and constant phenol conversion (~77.4 %) and H_2 yield (~58 %) were achieved. Similar trends are observed for the CO and CO_2 yields obtained with TOS during the in-situ pyrolysis-catalytic steam reforming reaction of PS dissolved in phenol. The high γ-Al_2O_3 concentration may contribute to the stability of the 2Ca3Al catalyst by assisting in the activation of CO_2 to produce reactive carbonates. As a result, more oxygen is available, which causes carbon to oxidize and prevents coke formation. Due to the creation of an alloy with other basic oxides in 2Ca3Al, which produces a C-O bond and surface carbon oxidation, the major factor limiting catalytic deactivation by basic catalysts may be attributed to this compound. Regarding the production of the H_2 and CO_2 yields with time on stream, it is evident that they decline with increasing time on stream at any pyrolysis temperature because the amount of the WGS and steam reforming processes is reduced when the reforming catalyst is deactivated. Interestingly, the reaction temperature affects the trend in the CO yield. Furthermore, due to the equilibrium between the attenuation of the reforming and WGS processes and the augmentation of the cracking reactions, catalyst deactivation has no appreciable impact on the CO yield in the reforming of the volatiles produced at 500 °C.

3.3. Characterization of the liquid product

A range of composite materials that can't be examined using conventional GC-FID can be characterized using Pyrolysis GC/MS because it is a useful tool for rapidly analyzing the catalytic pyrolysis products. Fig. 16 illustrates the primary condensed liquid products resulting from the in-situ pyrolysis-catalytic steam reforming reaction of the PS-phenol reforming reaction, as identified by their significant peaks and corresponding retention times in the GC/MS chromatogram for the 2Ca3Al sample. It is worth noting that this analysis was conducted using a minute sample size of only 0.05 g. The total ion chromatogram analysis identified seven main chemicals based on their relative peak area percentage and similarity to the library match. Hydroperoxides, aromatic, aliphatic, and alkane compounds were found in the liquid produced by catalytic pyrolysis. The 2Ca3Al nanocatalyst with high Lewis and Brønsted basic sites and moderated Brönsted and Lewis acid sites favored the conversion of Phenol and PS mixture into hydroperoxides, aliphatic and alkane hydrocarbon, resulting in the highest conversion rate. The first aliphatic primary amine was detected at 1.36 retention time and belonged to the methylamine (0.14 %) compound. The highest detected organic compound with a mass of 77.4 % was attributed to tert-Butyl Hydroperoxide (TBH). The third compound at 2.59 min of retention time belonged to the alkane category of 2-Methylhexane (0.16 %), an isomer of heptane. Most investigations on catalytic cracking, vapor-liquid phase equilibrium of heptane isomers, and iso-alkane oxidation employ 2-methylhexane as a model iso-alkane. The second highest detected component in the liquid products is Dixanthogen (21.2 %) which belongs to the class of organic compounds known as organic disulfides. The small percentage of aromatic 3-[3,5-bis(trifluoromethyl-phenylamino]-1-(4-fluorophenyl)-Propenone (BTFP) (0.09 %), p-Octiphenyl (0.07 %), and Palladium, [1,8-bis(diphenylphosphino)-9-anthracenyl-C,P,P']chloro-, (sp-4–3)- (BDAC) (0.07 %) were found in the liquid product. The two primary applications for p-Octiphenyl are manufacturing octylphenol ethoxylates and phenol/formaldehyde resins as an intermediary. As a result, value-added liquid components could also be produced from the in-situ pyrolysis-catalytic steam reforming reaction of PS dissolved in phenol, and the FTIR technique further characterized those products in Fig. 17.

The FTIR results of the pyrolysis liquid product coupled with the peak intensities, are displayed in Fig. 17 and may be used to determine the chemical bonds present in a molecule. The corresponding band at 440 cm^{-1} and 470 cm^{-1} are related to the stretching and deformation vibrations of S–O–S bonds, while a peak at 501 cm^{-1} is attributed to ν (C–C) mode and –S–S– bond stretching. Due to the breakdown and restructuring of carbon-containing oxygen groups, C−H bonds, and C−O bonds and the loss of macromolecules such as proteins, hemicellulose, and cellulose, the typical CO_2 peaks first emerged at a wavenumber of 787 cm^{-1} [78]. Because of the ring-opening or pyrolysis process, the intensity of the C–H out-of-plane bending characteristic peak of aromatic hydrocarbons and their derivatives at 787 cm1 was poor. The peak at wavenumber 903 cm^{-1} is because of the C−O−C symmetric stretch absorption. These peaks (903 cm^{-1}, 787 cm^{-1}, 440 cm^{-1}, and 470 cm^{-1}) also confirmed the presence of an aromatic compound in the pyrolytic products. Hydroperoxides are found at the small peak of 890 cm^{-1}, which corresponds with the region of O−O stretching vibration [79]. The bands (ν) at 1096 cm^{-1} correspond to the –C–O stretching vibration of ester groups [80] and C−F stretching of fluoro

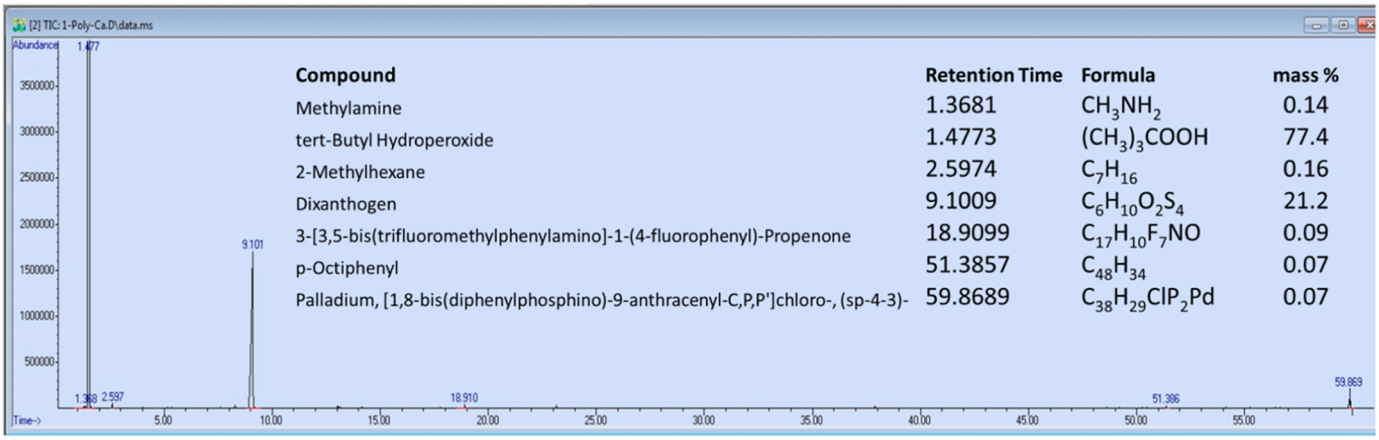

Fig. 16. GCMS data of pyrolytic products.

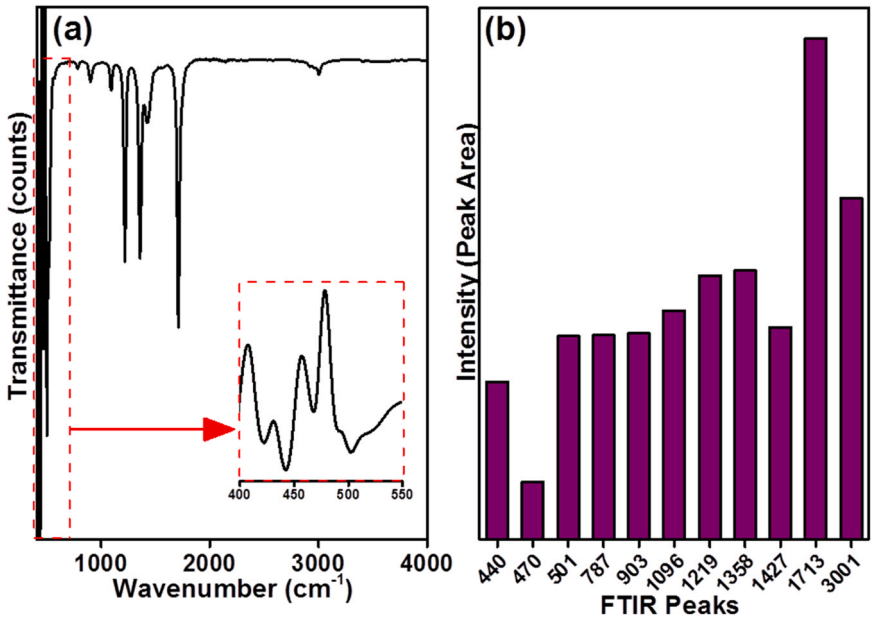

Fig. 17. FTIR curves of the pyrolysis liquid product alongside the band intensities according to peak areas.

compound, while transmittance peaks at 1219 cm^{-1} could be assigned to the –COH functional group of phenolic compounds [81]. The bands at 1358 cm^{-1} and 1427 cm^{-1} were assigned to the aromatic C═C absorption [82] and O–H bending vibration [83], respectively. The characteristic peak at 1713 cm^{-1} wavenumber could match the C═O stretching vibration of ketones, aldehydes, or esters [84], while the transmittance peak at 3001 cm^{-1} is assigned to the N-H stretching vibration of primary aliphatic amine. The above results proposed that liquid products primarily comprised aromatic hydrocarbons, phenols, hydroperoxides, and alkanes.

3.4. Post-reaction characterization

Catalysts might lose their catalytic activity, usually through poisoning from metal impurities, coke formation, high temperature, time, steam, and physical losses. It is crucial to analyze the spent catalysts because the abovementioned factors account for the inhibitions in catalytic performance. Thus, several characterizations, including TGA, BET surface area, N_2 adsorption-desorption isotherms, pore size distribution, TEM, CHNS, FTIR-KBr, SEM, EDX, and Elemental mapping analysis, were employed to investigate the physic-chemical properties of the spent catalysts. The TGA-DTG and CHNS findings of the used catalysts are shown in Fig. 18 and Table 2. The TGA pattern indicates that the weight loss may be separated into three zones due to the elimination of diverse species accumulated on the surface of the spent catalyst. As shown from the TGA profiles, up to 200 °C, the preliminary weight losses (WL_1) were due to the discharge of vapor molecules, carbon dioxide, or volatile constituents adsorbed on the catalyst surfaces. It can be seen that a very small amount of moisture is present for the 2Ca3Al sample (0.2 % of weight loss) with the lowest intense DTG peak at 62 °C and 102 °C, which reflects in the catalyst activity results too that the catalyst is well functioning with high basicity and low acidity. The second weight loss (WL_2) in the range of 200 °C and 600 °C relates to the removal of less stable deposits ("soft" coke) and could be ascribed to the relatively active amorphous carbon. As displayed in Fig. 18 and Table 2, the TGA curve of the spent Ca, 2Ca2Al, and 2Ca3Al samples, with the most intense DTG peaks for the Ca and 2Ca2Al samples, confirmed the existence of amorphous carbons with the weight losses of 17.8 %, 9.9 %, and 4.7 %, respectively. Weight loss above 600 °C (WL_3) can be ascribed to the removal of highly stable cokes ("hard" coke). Aliphatic carbonaceous was responsible for the "soft" coke species, whereas polycondensed aromatics were responsible for the "hard" coke species [85].

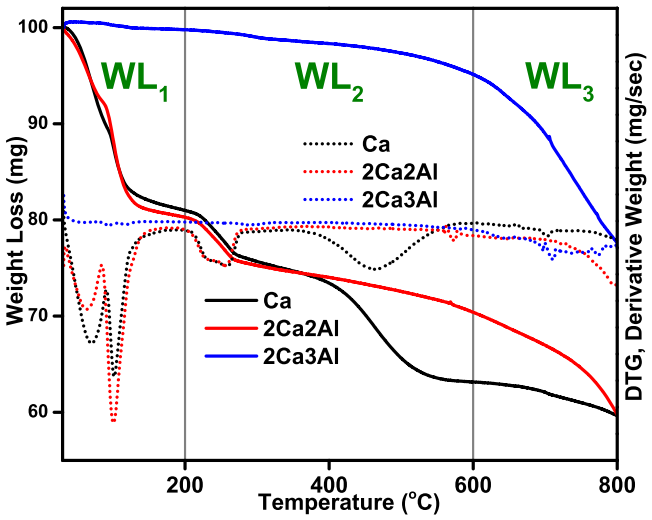

Fig. 18. TGA and DTG profiles of used catalysts.

The modest DTG peak of about 700 °C is ascribed explicitly to the breakdown of CaO carbonates (i.e., $CaCO_3$ oxycarbonate species) rather than the synthesis of graphitic carbon, as is the case for all samples. In general, the amount of deposited coke is in the sequence order: Ca < 2Ca2Al < 2Ca3Al following the TGA and CHNS results. As the γ-Al_2O_3 loading was increased, the amount of coking was reduced. The lower weight loss of the catalyst indicated high catalytic activity due to good metal–support interactions, high surface area, and strong basic sites. As the loading of γ-Al_2O_3 nanoparticles increases, the catalysts' acidity decreases (as shown by acidity results in Fig. 8 and.

Fig. 9), and more reducible metal species become available. According to previous research [86], the strength and concentration of the catalyst acid sites grow with coking's extent and rapidity. The γ-Al_2O_3 strengthened the channel blockage brought on by the condensation of macromolecular compounds on the surface by lowering the density of acid sites for the 2Ca3Al nanocatalysts channel expansion boosted mass transfer, reducing the local concentration of the coke precursors. In addition, the less water produced from the reaction for the Ca and 2Ca2Al samples avoids the excessive self-gasification of the γ-Al_2O_3 and CaO nanomaterial, and therefore, a serious weight losses are is shown in the TGA curve of spent Ca (40.4 %) and 2Ca2Al (40.3 %). The coke species on the used 2Ca3Al catalyst was further characterized by TEM (Fig. 21) and EDX (Fig. 22) spectroscopy.

N_2 adsorption-desorption analysis was used to examine the textural properties of the used catalysts, as shown in Fig. 19. The quantitative data of the spent S_{BET}, pore volume, and pore diameters of all samples are depicted in Table 2. Due to the coke obstructing certain active particles, the BET surface area of all spent samples was reduced compared to the fresh ones in different amounts. The results showed that the spent catalyst with high γ-Al_2O_3 content still possessed the highest surface area (50.11 m^2/g) dispersion, the largest particle size (22.77 nm), and a more intense STP with H3 isotherm loop, which is in agreement with the results obtained from fresh characterization tests. The findings also imply that no considerable sintering had occurred (especially for the spent 2Ca3Al sample), as sintering resulted in an apparent reduction of surface area. Consequently, there is a direct correlation between the activity and textural attributes. The only spent sample with enough surface area and pore volume to activate phenol and spread the reactants and products throughout the crystal was 2Ca3Al. Due to the obstruction of carbon deposition in micropores, the Ca and 2Ca2Al exhibit a tight hysteresis loop with Type H3 isotherm, lower relative pressure (P/Po), lower STP, and reduced pore size distribution in contrast to fresh catalysts. These findings also suggest that Al NPs containing catalysts are more competitive in restoring the textural properties of used samples. After the reaction, the data showed that the H3-

Table 2
Weight loss, surface area, and carbon contents of the spent nano-sized catalysts.

Catalysts	Weight loss (%)			Total weight loss (%)	Fresh catalyst Surface area (m^2/g)	Spent catalyst Surface area (m^2/g)	Pore-volume ($cm^3.g^{-1}$)	Pore-diameter (nm)	Carbon Content (wt %)[a]
	WL_1	WL_2	WL_3						
Ca	19.1	17.8	3.5	40.4	13.76	27.00	0.117	17.27	7.2
2Ca2Al	19.7	9.9	10.7	40.3	64.59	46.34	0.168	14.49	6.9
2Ca3Al	0.2	4.7	17.5	22.4	72.39	50.11	0.285	22.77	2.4

[c] Carbon wt % was determined by CHNS elemental analysis

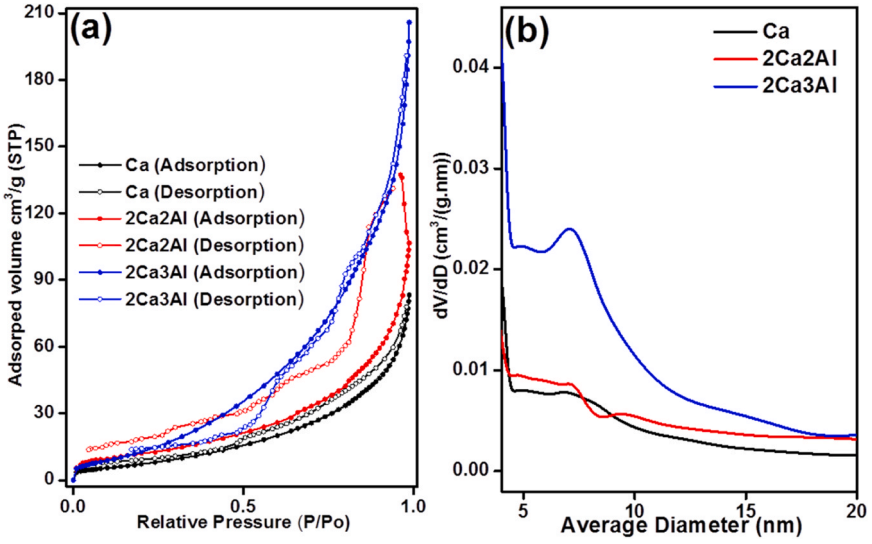

Fig. 19. (a) N_2 adsorption-desorption isotherms and (b) pore size distribution plots of the spent catalysts.

type isotherms loop remained intact for all catalysts, indicating no significant collapse of the mesoporous framework. According to these findings, adding γ-Al_2O_3 in a specific amount helps the catalyst maintain its activity and enhances its anti-coking capabilities.

To further characterize the structure and properties of carbon deposition and functional group presented in the used catalysts, we conducted the FTIR-KBr analysis in the range of 4000−400 cm^{-1}, and the results are depicted in Fig. 20. By analyzing the FTIR spectra of the fresh (Fig. 9) and used (Fig. 17) catalysts, we could identify the functional groups present in each sample and compare their spectral profiles. The general FTIR profile for the fresh and used catalysts exhibited comparable features, indicating that the fundamental chemical composition of the materials had not undergone significant changes. However, the used catalysts exhibited more vibrational and fluctuation characteristics in their FTIR curves than the fresh catalysts. It was postulated that these alterations were likely due to coke deposition, which refers to the accumulation of carbon-based compounds on the catalyst's surface. The Ca–O− rocking mode was observed at 540 cm^{-1}, while the peak at 1010 cm^{-1} is due to the asymmetric stretching mode of C–O–C. The broad characteristic FTIR peaks located at 1412 cm^{-1} represent the existent of nitrates, and C-N, N-H, and C-H bonds [87], whereas the peak at 1651 cm^{-1} signifies the stretching vibration of C═O and C═N groups [88]. The FTIR characteristic bands at 2369 cm^{-1}, 3456 cm^{-1} and 3757 cm^{-1} are attributed mainly to C≡N deformation, the O-H stretching vibration of the surface hydroxyl group, and the stretching mode of the OH^-, respectively. To conclude, no significant changes and destruction in band position between spent catalysts are observed, which indicates the in-situ pyrolysis-catalytic steam reforming reaction of PS dissolved in phenol did not affect the structure of Ca, 2Ca2Al and 2Ca3Al nanocatalysts.

To gain insight into the impact of textural properties on the morphology of carbonaceous species deposited on the catalyst, the spent catalysts obtained after the screening process (before the stability test) were analyzed employing transmission electron microscopy (TEM), and the findings are presented in Fig. 21. The morphologies of the coke produced from the experiments mainly include amorphous coke and carbon nanofiber (CNFs) deposited on the 2Ca3Al surface. TEM micrographs of spent 2Ca3Al catalyst also reveal the presence of carbon deposits with filamentous type was observed as expected from the TGA and CHNS patterns. The TEM images of 2Ca3Al clearly illustrate the development of well-ordered mesopores, the production of nearly two layers of graphitic carbon on the catalyst's surface, and no severe sintering of Ca and Al particles on the spent sample was observed. However, there is

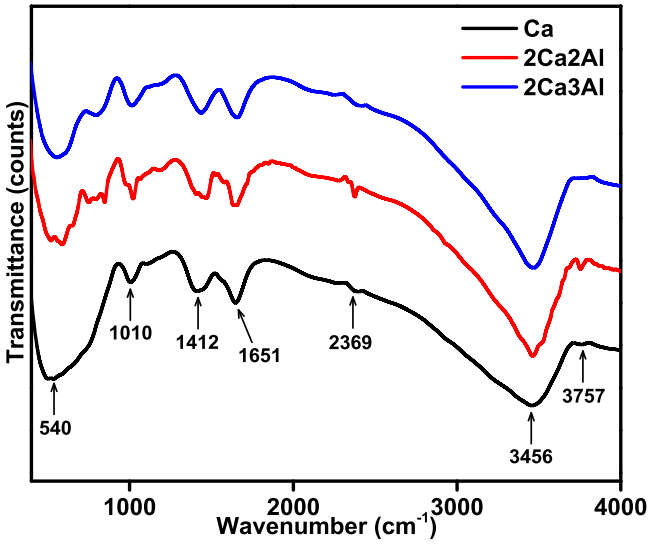

Fig. 20. FTIR-KBr curves of used catalysts.

proof that carbon nanofilament development over the catalyst might result in reactor clogging rather than catalyst deactivation [89]. The shell-shaped coke enclosed on the metal nanoparticles of the used catalyst with around 50 nm graphitic carbon layers is seen from the inset in the images and proves the effective synthesis of a sandwich-type catalyst. It was widely believed that oxygen vacancies in catalyst particle shells might speed up the in-situ gasification of coke by facilitating the adsorption and activation of CO_2 to create the mobile O species [90]. The core-shell structure of the spent 2Ca3Al nanocatalyst can entirely inhibit reaction molecules and medium from interacting with the metal's core, shielding the core from corrosion, oxidation, or sintering.

The SEM and EDX images of the spent 2Ca3Al and best-performing catalyst were investigated for carbon deposition. The SEM image after the catalyst screening (before the stability test) presented in Fig. 22 showed that the 2Ca3Al catalyst formed carbon with a grained surface had been observed. This detrimental effect affects catalytic activity by including the catalyst's active areas. Catalysts using CaO particles lessen carbon deposition, perhaps preventing the formation of carbonates [91]. The effective suppression of carbon caused by CaO-based bifunctional materials with mixed metallic oxides has also recently been discussed in the literature [92]. The image depicts the C signal as heterogeneous in contrast to the more homogenous distribution of the carbon. Regions with a high concentration of coke can be observed close to areas that are comparatively low in coke deposition. EDX line scans and mappings were performed to confirm all Al and Ca nanoparticles were still well-confined within the 2Ca3Al shells. This could be because, on the one hand, the Al and Ca nanoparticles are oxidized. On the other hand, some of the lattice oxygen in the hydroxyapatite is consumed during cracking and reforming. It is replaced in the air environment in the TGA tests. The mass gain from the oxidation of aluminum and calcium as well as the recovery of lattice oxygen, outweighs the mass loss from the oxidation of carbon, to put it simply.

4. Conclusion

The current research focused on synthesizing a potential precious metal-free Ca-Al nanocatalyst with excellent catalytic activity and strong coke resistance. Three catalysts, namely Ca, 2Ca2Al, and 2Ca3Al, were synthesized by impregnation and hydrothermal methods and characterized by N_2 adsorption-desorption isotherms, BET surface area, TEM, SEM, EDX element mapping analysis, XRD, FTIR-KBr, CO_2-TPD, pyrrole- TGA-DTG, pyrrole-FTIR spectra, pyridine FTIR spectra, and pyridine TGA-DTG, and H_2-TPR. GC-TCD analyzed the gas products, and liquid products were analyzed by GC/MS, GC-FID, and FTIR. Spent CHNS, TGA-DTG, FTIR-KBr, N_2 adsorption-desorption isotherms, BET surface area, SEM, EDX, and TEM analysis also examined samples. The current study on the surface properties and activity of the catalyst indicates the significant role of a synergistic effect of catalyst basicity, high surface area, and reducibility in improving the in-situ pyrolysis-catalytic steam reforming reaction of PS dissolved in the phenol process. Additionally, RWGS was crucial to the in-situ pyrolysis-catalytic steam reforming reaction of PS dissolved in phenol. Both are connected to the surface properties: the basic sites are preferred for RWGS and improve the catalytic performance. The typical 2Ca3Al nanocatalyst with high γ-Al_2O_3 content performed the best in H_2 yield and phenol conversion during testing. The amount, kind, and placement of coke in the catalyst particles, which are determined using various methodologies, affect the conversion's time-on-stream development and the yields of its products. Nevertheless, the coke formation was mainly influenced by the catalyst's acidity; therefore, the catalysts with the higher acidity contents showed weaker resistance against coke formation. Thus, the spent 2Ca3Al nanocatalyst with a high basic site and low acidity exhibited negligible carbon formation on the catalyst surface. The obtained phenol conversion and H_2 yield of the 2Ca3Al nanocatalyst at 700 ^oC were 98.5 % and 92.5 %, respectively. The 2Ca3Al nanocatalyst was tested for 50 h of TOS at 500 ^oC and found to be highly stable. The core-shell structure of

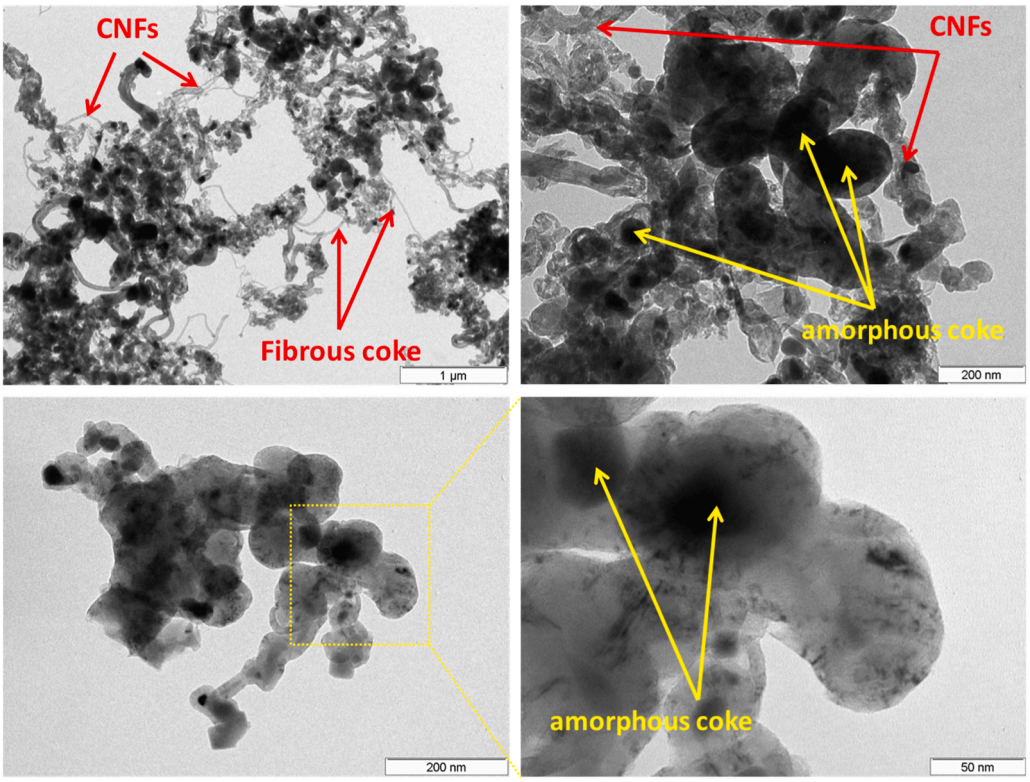

Fig. 21. TEM images of the used 2Ca3Al nano-catalysts.

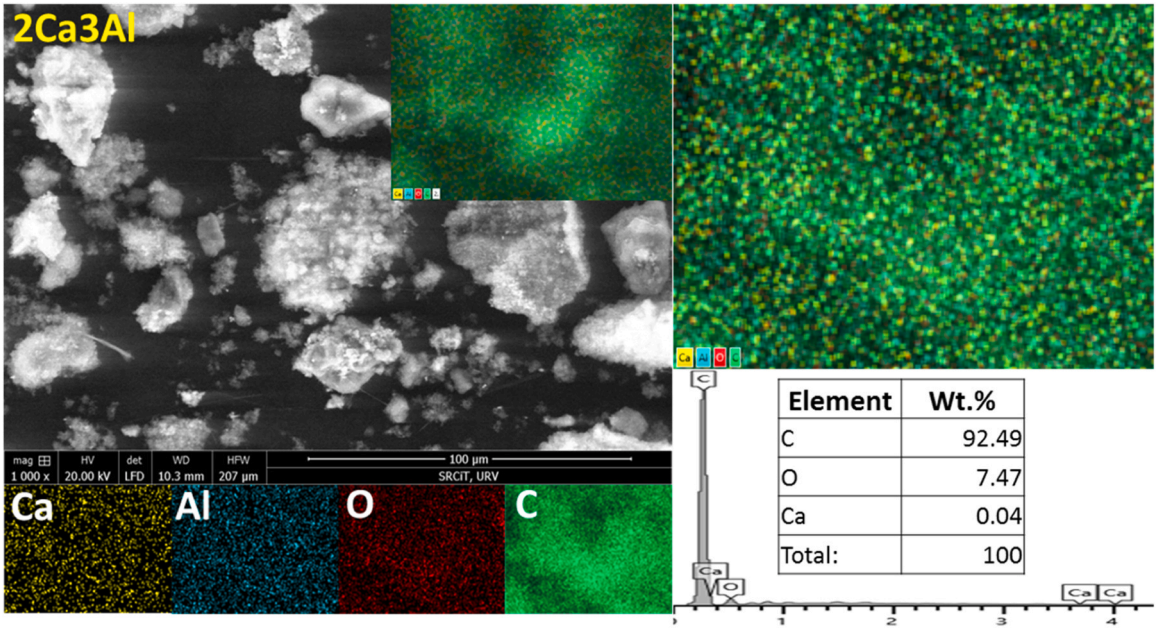

Fig. 22. SEM, EDX and Elemental mapping analysis of the spent 2Ca3Al nanocatalyst.

the 2Ca3Al nanocatalyst successfully increased the H_2 generation and decreased the undesirable products, according to the TEM results of the used catalysts. This structure also avoided the sintering and oxidation of nanoparticles. The liquid products were composed of methylamine, TBH, 2-Methylhexane, Dixanthogen, BTFP, p-Octiphenyl, and BDAC. The current investigation helps inspire institutes and industries to cogenerate valuable liquid and gas products from the in-situ catalytic pyrolysis steam reforming of PS plastic wastes and develop feasible technologies such as pilot scale PBR for a high rate of plastic recycling.

CRediT authorship contribution statement

W. Nabgan: Investigation, Writing – original draft preparation, Visualization Mohd Zahid Ansari: Methodology, Formal analysis, Writing – review and editing M. Ikram: Conceptualization, Resources H. Alqaraghuli: Conceptualization, Writing – review and editing, Investigation L. Parashuram: Methodology, Formal analysis Thuan Van Tran: Data Curation, Resources Mohammed A. Amin: Formal analysis, Conceptualization, Funding acquisition T.A. Tuan Abdullah:

interpretation, conceptualization, Resources, Methodology Ridha Djellabi: Conceptualization, Formal analysis, Writing – review and editing F. Medina: Supervision, fund acquisition A.A. Jalil: data analysis, Resources, Methodology.

Declaration of Competing Interest

The authors declare that they have no known competing financial interests or personal relationships that could have appeared to influence the work reported in this paper.

Data Availability

Data will be made available on request.

Acknowledgments

The principal author, Walid Nabgan, is thankful for the support from Universitat Rovira i Virgili under the Maria Zambrano Programme (Reference number: 2021URV-MZ-10), Proyectos de Generación de Conocimiento AEI/MCIN (PID2021–123665OB-I00), and the project reference number of TED2021–129343B-I00. The authors are also grateful for the support given by Universiti Teknologi Malaysia (UTM) allocation budget in Pusat Pengurusan Makmal Universiti (PPMU) laboratory. The researchers would also like to acknowledge the Deanship of Scientific Research, Taif University for funding this work.

References

[1] S. Czernik, R.J. French, Energy Fuels 20 (2006) 754–758.
[2] T. Namioka, A. Saito, Y. Inoue, Y. Park, T.-j Min, S.-a Roh, K. Yoshikawa, Hydrogen-rich gas production from waste plastics by pyrolysis and low-temperature steam reforming over a ruthenium catalyst, Appl. Energy 88 (2011) 2019–2026.
[3] L. Santamaria, G. Lopez, E. Fernandez, M. Cortazar, A. Arregi, M. Olazar, J. Bilbao, Progress on catalyst development for the steam reforming of biomass and waste plastics pyrolysis volatiles: a review, Energy Fuels 35 (2021) 17051–17084.
[4] I. Barbarias, G. Lopez, M. Artetxe, A. Arregi, L. Santamaria, J. Bilbao, M. Olazar, Pyrolysis and in-line catalytic steam reforming of polystyrene through a two-step reaction system, J. Anal. Appl. Pyrolysis 122 (2016) 502–510.
[5] C. Wu, P.T. Williams, Pyrolysis–gasification of plastics, mixed plastics and real-world plastic waste with and without Ni–Mg–Al catalyst, Fuel 89 (2010) 3022–3032.
[6] Y. Liu, K. Chandra Akula, K. Phani Raj Dandamudi, Y. Liu, M. Xu, A. Sanchez, D. Zhu, S. Deng, Effective depolymerization of polyethylene plastic wastes under hydrothermal and solvothermal liquefaction conditions, Chem. Eng. J. 446 (2022), 137238.
[7] P. Manuel, M. Almeida, M. Martins, M. Oliveira, Effects of nanoplastics on zebrafish embryo-larval stages: a case study with polystyrene (PS) and polymethylmethacrylate (PMMA) particles, Environ. Res. 213 (2022), 113584.
[8] Y. Li, X. Li, P. Wang, Y. Su, B. Xie, The effects of biochar and its applications in the microbial remediation of contaminated soil: a review, J. Hazard. Mater. 438 (2022), 129493.
[9] Z. Xu, F. Pan, M. Sun, J. Xu, N.E. Munyaneza, Z.L. Croft, G. Cai, G. Liu, Proc. Natl. Acad. Sci. 119 (2022) e2203346119.
[10] J. Scheirs, W. Kaminsky, Feedstock Recycling and Pyrolysis of Waste Plastics: Converting Waste Plastics Into Diesel and Other Fuels, J. Wiley & Sons, 2006.
[11] E. Butler, G. Devlin, K. McDonnell, Waste polyolefins to liquid fuels via pyrolysis: review of commercial state-of-the-art and recent laboratory research, Waste Biomass. Valoriz. 2 (2011) 227–255.
[12] D. Damayanti, D.R. Saputri, D.S. Marpaung, F. Yusupandi, A. Sanjaya, Y. M. Simbolon, W. Asmarani, M. Ulfa, H.-S. Wu, Current prospects for plastic waste treatment, Polymers 14 (15) (2022), 3133.
[13] W. Nabgan, T.A. Tuan Abdullah, R. Mat, B. Nabgan, Y. Gambo, M. Ibrahim, A. Ahmad, A.A. Jalil, S. Triwahyono, I. Saeh, Renewable hydrogen production from bio-oil derivative via catalytic steam reforming: an overview, Renew. Sustain. Energy Rev. 79 (2017) 347–357.
[14] L.M.J. Sprakel, G. Bargeman, L. Galan Sanchez, B. Schuur, J. Chem. Technol. Biotechnol. 96 (2021) 1918–1926.
[15] C. Berrueco, F.J. Mastral, E. Esperanza, J. Ceamanos, Energy Fuels 16 (2002) 1148–1153.
[16] M. Della Zassa, M. Favero, P. Canu, Two-steps selective thermal depolymerization of polyethylene. 1: feasibility and effect of devolatilization heating policy, J. Anal. Appl. Pyrolysis 87 (2010) 248–255.
[17] N. Miskolczi, A. Angyal, L. Bartha, I. Valkai, Fuels by pyrolysis of waste plastics from agricultural and packaging sectors in a pilot scale reactor, Fuel Process. Technol. 90 (2009) 1032–1040.
[18] Y. Park, T. Namioka, S. Sakamoto, T.-j Min, S.-a Roh, K. Yoshikawa, Optimum operating conditions for a two-stage gasification process fueled by polypropylene by means of continuous reactor over ruthenium catalyst, Fuel Process. Technol. 91 (2010) 951–957.
[19] W. Nabgan, B. Nabgan, T.A. Tuan Abdullah, M. Ikram, A.H. Jadhav, A.A. Jalil, M. W. Ali, Highly active biphasic anatase-rutile Ni-Pd/TNPs nanocatalyst for the reforming and cracking reactions of microplastic waste dissolved in phenol, ACS Omega 7 (2022) 3324–3340.
[20] W. Nabgan, B. Nabgan, T.A.T. Abdullah, M. Ikram, A.H. Jadhav, M.W. Ali, A. A. Jalil, Hydrogen and value-added liquid fuel generation from pyrolysis-catalytic steam reforming conditions of microplastics waste dissolved in phenol over bifunctional Ni-Pt supported on Ti-Al nanocatalysts, Catal. Today 400–401 (2022) 35–48.
[21] W. Nabgan, T.A. Tuan Abdullah, R. Mat, B. Nabgan, S. Triwahyono, A. Ripin, Hydrogen production from catalytic steam reforming of phenol with bimetallic nickel-cobalt catalyst on various supports, Appl. Catal. A: Gen. 527 (2016) 161–170.
[22] S. Velu, K. Suzuki, C.S. Gopinath, Photoemission and in Situ XRD investigations on CuCoZnAl-mixed metal oxide catalysts for the oxidative steam reforming of methanol, J. Phys. Chem. B 106 (2002) 12737–12746.
[23] Q. Peng, Y. Tao, H. Ling, Z. Wu, Z. Zhu, R. Jiang, Y. Zhao, Y. Wang, C. Ji, X. Liao, A. Vassallo, J. Huang, ACS Sustain. Chem. Eng. 5 (2017) 2098–2108.
[24] C. Dang, S. Wu, G. Yang, Y. Cao, H. Wang, F. Peng, S. Wang, H. Yu, ACS Sustain. Chem. Eng. 8 (2020) 7111–7120.
[25] D.A. Constantinou, M.C. Álvarez-Galván, J.L.G. Fierro, A.M. Efstathiou, Low-temperature conversion of phenol into CO, CO_2 and H2 by steam reforming over La-containing supported Rh catalysts, Appl. Catal. B: Environ. 117-118 (2012) 81–95.
[26] G. Zhang, in: A.M.A. Asiri, A. Khan, S.A. Bhawani, B.M.M. Abu-Zied, S. Siengchin, H. Džudžević-Čančar (Eds.), Carbon-Based Metal Free Catalysts, Elsevier, 2022, pp. 21–66.
[27] A.M. Pennington, R.A. Yang, D.T. Munoz, F.E. Celik, Metal-free hydrogen evolution over defect-rich anatase titanium dioxide, Int. J. Hydrog. Energy 43 (2018) 15176–15190.
[28] A. Caglar, T.A. Hansu, H. Demir-Kivrak, in: A.M.A. Asiri, A. Khan, S.A. Bhawani, B. M.M. Abu-Zied, S. Siengchin, H. Džudžević-Čančar (Eds.), Carbon-Based Metal Free Catalysts, Elsevier, 2022, pp. 111–136.
[29] P. Nkulikiyinka, S.T. Wagland, V. Manovic, P.T. Clough, Prediction of combined sorbent and catalyst materials for SE-SMR, using QSPR and multitask learning, Ind. Eng. Chem. Res. 61 (2022) 9218–9233.
[30] G. Xu, T. Murakami, T. Suda, S. Kusama, T. Fujimori, Ind. Eng. Chem. Res. 44 (2005) 5864–5868.
[31] M.A. Ashraf, O. Sanz, C. Italiano, A. Vita, M. Montes, S. Specchia, Analysis of Ru/La-Al2O3 catalyst loading on alumina monoliths and controlling regimes in methane steam reforming, Chem. Eng. J. 334 (2018) 1792–1807.
[32] W. Xie, Y. Sun, H. Liu, H. Fu, Y. Liang, Calcium-ion-triggered co-assembly of peptide and polysaccharide into a hybrid hydrogel for drug delivery, Appl. Surf. Sci. 360 (2016) 184–191.
[33] M.H. Aboonasr Shiraz, M. Rezaei, F. Meshkani, Microemulsion synthesis method for preparation of mesoporous nanocrystalline γ-Al2O3 powders as catalyst carrier for nickel catalyst in dry reforming reaction, Int. J. Hydrog. Energy 41 (2016) 6353–6361.
[34] W. Nabgan, B. Nabgan, T.A. Tuan Abdullah, N. Ngadi, A.A. Jalil, N.S. Hassan, S. M. Izan, W.S. Luing, S.N. Abdullah, F.S.A. Majeed, Conversion of polyethylene terephthalate plastic waste and phenol steam reforming to hydrogen and valuable liquid fuel: synthesis effect of Ni–Co/ZrO2 nanostructured catalysts, Int. J. Hydrog. Energy 45 (2020) 6302–6317.
[35] W. Nabgan, B. Nabgan, T.A. Tuan Abdullah, A.A. Jalil, A. Ul-Hamid, M. Ikram, A. H. Nordin, A. Coelho, Production of hydrogen and valuable fuels from polyethylene terephthalate waste dissolved in phenol reforming and cracking reactions via Ni-Co/CeO2 nano-catalyst, J. Anal. Appl. Pyrolysis 154 (2021), 105018.
[36] J.H. Park, C. Park, K.S. Lee, S.J. Suh, AIP Adv. 10 (2020), 115220.
[37] M.Y.S. Hamid, M.L. Firmansyah, S. Triwahyono, A.A. Jalil, R.R. Mukti, E. Febriyanti, V. Suendo, H.D. Setiabudi, M. Mohamed, W. Nabgan, Oxygen vacancy-rich mesoporous silica KCC-1 for CO 2 methanation, Appl. Catal. A: Gen. 532 (2017) 86–94.
[38] S.N. Bukhari, C.C. Chong, H.D. Setiabudi, Y.W. Cheng, L.P. Teh, A.A. Jalil, Ni/Fibrous type SBA-15: highly active and coke resistant catalyst for CO_2 methanation, Chem. Eng. Sci. 229 (2021), 116141.
[39] S. Triwahyono, A.A. Jalil, M. Musthofa, Generation of protonic acid sites from pentane on the surfaces of Pt/SO42−-ZrO2 and Zn/H-ZSM5 evidenced by IR study of adsorbed pyridine, Appl. Catal. A: Gen. 372 (2010) 90–93.
[40] T.J. Siang, A.A. Jalil, M.Y.S. Hamid, Bifunctional metal-free KAUST catalysis center 1 (KCC-1) as highly active catalyst for syngas production via methane partial oxidation, Mater. Today Chem. 23 (2022), 100684.
[41] W. Nabgan, T.A. Tuan Abdullah, R. Mat, B. Nabgan, Y. Gambo, K. Moghadamian, Acetic acid-phenol steam reforming for hydrogen production: effect of different composition of La2O3-Al2O3 support for bimetallic Ni-Co catalyst, J. Environ. Chem. Eng. 4 (2016) 2765–2773.
[42] W. Nabgan, T.A. Tuan Abdullah, R. Mat, B. Nabgan, Y. Gambo, S. Triwahyono, Influence of Ni to Co ratio supported on ZrO2 catalysts in phenol steam reforming for hydrogen production, Int. J. Hydrog. Energy 41 (2016) 22922–22931.
[43] B. Nabgan, M. Tahir, T.A.T. Abdullah, W. Nabgan, Y. Gambo, R. Mat, I. Saeh, Ni/Pd-promoted Al 2 O 3 –La 2 O 3 catalyst for hydrogen production from

polyethylene terephthalate waste via steam reforming, Int. J. Hydrog. Energy 42 (2017) 10708–10721.
[44] J.D.A. Bellido, J.E. De Souza, J.-C. M'Peko, E.M. Assaf, Effect of adding CaO to ZrO2 support on nickel catalyst activity in dry reforming of methane, Appl. Catal. A: Gen. 358 (2009) 215–223.
[45] A.M. Kalinkin, E.V. Kalinkina, O.A. Zalkind, T.I. Makarova, Chemical interaction of calcium oxide and calcium hydroxide with CO_2 during mechanical activation, Inorg. Mater. 41 (2005) 1073–1079.
[46] A.M. Bruno, T.D.R. Simões, M.M.V.M. Souza, R.L. Manfro, Cu catalysts supported on CaO/MgO for glycerol conversion to lactic acid in alkaline medium employing a continuous flow reaction system, RSC Adv. 10 (2020) 31123–31138.
[47] J. Akil, S. Siffert, P.-R. Laurence, D.P. Debecker, F. Devred, R. Cousin, C. Poupin, Effect of precious metals on NO reduction by CO in oxidative conditions, Appl. Sci. 10 (2020) 3042.
[48] Z.A. Alothman, A review: fundamental aspects of silicate mesoporous materials, Materials 5 (2012) 2874–2902.
[49] S. Yurdakal, C. Garlisi, L. Özcan, M. Bellardita, G. Palmisano, in: G. Marcì, L. Palmisano (Eds.), Heterogeneous Photocatalysis, Elsevier, 2019, pp. 87–152.
[50] J. Hu, P. Hongmanorom, P. Chirawatkul, S. Kawi, Chem. Eng. J. 426 (2021), 130864.
[51] S. Kwon, H.J. Kwon, J.I. Choi, H.C. Lee, A.G. Russell, S.G. Lee, T. Kim, S.S. Jang, Toward enhanced CO_2 adsorption on bimodal calcium-based materials with porous truncated architectures, Appl. Surf. Sci. 505 (2020), 144512.
[52] C. Yang, J. Wang, Q. Xu, A blind testing design for authenticating ancient DNA sequences, Microporous Mater. 11 (1997) 261–268.
[53] R. Trane, S. Dahl, M.S. Skjøth-Rasmussen, A.D. Jensen, Catalytic steam reforming of bio-oil, Int. J. Hydrog. Energy 37 (2012) 6447–6472.
[54] J. Chen, J. Sun, Y. Wang, DDX3 binding with CK1ε was closely related to motor neuron degeneration of ALS by affecting neurite outgrowth, Ind. Eng. Chem. Res. 56 (2017) 4627–4637.
[55] E.P. Parry, An infrared study of pyridine adsorbed on acidic solids. Characterization of surface acidity, J. Catal. 2 (1963) 371–379.
[56] I. Qoniah, D. Prasetyoko, H. Bahruji, S. Triwahyono, A.A. Jalil, Suprapto Hartati, T. E. Purbaningtias, Direct synthesis of mesoporous aluminosilicates from Indonesian kaolin clay without calcination, Appl. Clay Sci. 118 (2015) 290–294.
[57] W. Nabgan, T.A.T. Abdullah, M. Ikram, A.H.K. Owgi, A.H. Hatta, M. Alhassan, F.F. A. Aziz, A.A. Jalil, T. Van Tran, R. Djellabi, Hydrogen and valuable liquid fuel production from the in-situ pyrolysis-catalytic steam reforming reactions of cellulose bio-polymer wastes dissolved in phenol over trimetallic Ni-La-Pd/TiCa nanocatalysts, J. Environ. Chem. Eng. 11 (2023), 109311.
[58] H. Shahzad, M. Imran, A. Haider, S. Naz, E. Umar, A. Ul-Hamid, et al., Catalytic and antimicrobial properties of Ag and polyacrylic acid doped SrO nanocomposites; molecular docking analysis, Journal of Photochemistry and Photobiology A: Chemistry 444 (2023), 114970.
[59] V.K. Thakur, D. Vennerberg, M.R. Kessler, Green aqueous surface modification of polypropylene for novel polymer nanocomposites, ACS Appl. Mater. Interfaces 6 (2014) 9349–9356.
[60] J. Sala-Pala, J. Roue, J.E. Guerchals, Study of a new type of transition metal peroxo complexes as oxidants, J. Mol. Catal. 7 (1980) 141–148.
[61] F. Faccioli, M. Bauer, D. Pedron, A. Sorarù, M. Carraro, S. Gross, Hydrolytic stability and hydrogen peroxide activation of zirconium-based oxoclusters, Eur. J. Inorg. Chem. 2015 (2015) 210–225.
[62] K. Sobańska, P. Pietrzyk, Z. Sojka, Generation of reactive oxygen species via electroprotic interaction of H2O2with ZrO2Gel: ionic sponge effect and pH-switchable peroxidase- and catalase-like activity, ACS Catal. 7 (2017) 2935–2947.
[63] B.R. Ganapuram, M. Alle, R. Dadigala, A. Dasari, V. Maragoni, V. Guttena, Catalytic reduction of methylene blue and Congo red dyes using green synthesized gold nanoparticles capped by salmalia malabarica gum, Int. Nano Lett. 5 (2015) 215–222.
[64] C.H. Ali, A.H. Asif, T. Iqbal, A.S. Qureshi, M.A. Kazmi, S. Yasin, M. Danish, B.-Z. Mu, Improved transesterification of waste cooking oil into biodiesel using calcined goat bone as a catalyst, Energy Sources, Part A: Recovery, Util., Environ. Eff. 40 (2018) 1076–1083.
[65] W. Liu, Z. Ren, A.T. Bosse, K. Liao, E.L. Goldstein, J. Bacsa, D.G. Musaev, B. M. Stoltz, H.M.L. Davies, Catalyst-controlled selective functionalization of unactivated C-H bonds in the presence of electronically activated C-H bonds, J. Am. Chem. Soc. 140 (2018) 12247–12255.
[66] J. Hu, Y. Li, Y. Zhen, M. Chen, H. Wan, Comparison of cost-effectiveness and benefits of surgery-first versus orthodontics-first orthognathic correction of skeletal class III malocclusion, Chin. J. Catal. 42 (2021) 367–375.
[67] D. Pan, J. Chen, W. Tao, L. Nie, S. Yao, Polyoxometalate-modified carbon nanotubes: new catalyst support for methanol electro-oxidation, Langmuir 22 (2006) 5872–5876.
[68] C. Dai, Z. Zhou, C. Tian, Y. Li, C. Yang, X. Gao, X. Tian, Large-scale synthesis of graphene-like MoSe2nanosheets for efficient hydrogen evolution reaction, J. Phys. Chem. C 121 (2017) 1974–1981.
[69] R.B. Church, K. Hu, G. Magnacca, M. Cerruti, Intercalated species in multilayer graphene oxide: insights gained from in situ FTIR spectroscopy with probe molecule delivery, J. Phys. Chem. C 120 (2016) 23207–23211.
[70] N. Ma, Z. Hao, G. Liu, H. Zhang, S. Zhan, Mechanistic insight into the dynamic transformation of acid sites on ceria supported molybdenum oxide catalyst for NOx reduction, Journal of Environmental Chemical Engineering 10 (2022), 108114.
[71] E.C. Vagia, A.A. Lemonidou, Hydrogen production via steam reforming of bio-oil components over calcium aluminate supported nickel and noble metal catalysts, Appl. Catal. A: Gen. 351 (2008) 111–121.
[72] Y.S. Noh, K.-Y. Lee, D.J. Moon, Hydrogen production by steam reforming of methane over nickel based structured catalysts supported on calcium aluminate modified SiC, Int. J. Hydrog. Energy 44 (2019) 21010–21019.
[73] R. He, R.R. Davda, J.A. Dumesic, In situ ATR-IR spectroscopic and reaction kinetics studies of water-gas shift and methanol reforming on Pt/Al2O3 catalysts in vapor and liquid phases, J. Phys. Chem. B 109 (2005) 2810–2820.
[74] M.-L. Bailly, G. Costentin, H. Lauron-Pernot, J.M. Krafft, M. Che, Physicochemical and in situ photoluminescence study of the reversible transformation of oxide ions of low coordination into hydroxyl groups upon interaction of water and methanol with MgO, J. Phys. Chem. B 109 (2005) 2404–2413.
[75] Y. Guo, M.U. Azmat, X. Liu, Y. Wang, G. Lu, Effect of support's basic properties on hydrogen production in aqueous-phase reforming of glycerol and correlation between WGS and APR, Appl. Energy 92 (2012) 218–223.
[76] S. Wang, F. Zhang, Q. Cai, X. Li, L. Zhu, Q. Wang, et al., Catalytic steam reforming of bio-oil model compounds for hydrogen production over coal ash supported Ni catalyst, International Journal of Hydrogen Energy 39 (2014) 2018–2025.
[77] C. Dang, S. Liang, W. Yang, W. Cai, High-purity hydrogen production from phenol on Ni-CaO-Ca12Al14O33 multifunctional catalyst derived from recovered layered double hydroxide, Fuel 332 (2023), 126041, 126041.
[78] Z. Ni, H. Bi, C. Jiang, J. Tian, H. Sun, W. Zhou, Q. Lin, Research on the co-pyrolysis of coal gangue and coffee industry residue based on machine language: Interaction, kinetics, and thermodynamics, Sci. Total Environ. 804 (2022), 150217.
[79] A. Hemmingsen, J.T. Allen, S. Zhang, J. Mortensen, M.A. Spiteri, Early detection of ozone-induced hydroperoxides in epithelial cells by a novel infrared spectroscopic method, Free Radic. Res. 31 (1999) 437–448.
[80] J.J. Melchor, I.C.P. Fortes, Bio-oil production by pyrolysis of metal soaps derived from macauba pulp oil, J. Anal. Appl. Pyrolysis 135 (2018) 101–110.
[81] M.H. Tahir, T. Mubashir, M. Schulze, R.M. Irfan, International Journal of Energy Research n/a (2022).
[82] X.-F. Wu, J.-J. Zhang, Y.-H. Huang, M.-F. Li, J. Bian, F. Peng, Comparative investigation on bio-oil production from eucalyptus via liquefaction in subcritical water and supercritical ethanol, Ind. Crops Prod. 140 (2019), 111695.
[83] Y. Liu, Y. Song, C. Ran, A. Ali Siyal, Z. Jiang, P. Chtaeva, Z. Deng, T. Zhang, J. Fu, W. Ao, C. Zhou, X. Li, L. Wang, J. Dai, Characterization and analysis of condensates and non-condensable gases from furfural residue via fast pyrolysis in a bubbling fluidized bed reactor, Waste Manag. 125 (2021) 77–86.
[84] H. Jiang, W. Hong, Y. Zhang, S. Deng, J. Chen, C. Yang, H. Ding, Behavior, kinetic and product characteristics of the pyrolysis of oil shale catalyzed by cobalt-montmorillonite catalyst, Fuel 269 (2020), 117468.
[85] X.-Y. Ren, J.-P. Cao, Y. Li, Z.-M. He, X.-Y. Zhao, T.-L. Liu, X.-B. Feng, Y.-P. Zhao, H.-C. Bai, J. Zhang, S.-X. Zhao, Ind. Eng. Chem. Res. 60 (2021) 12521–12533.
[86] M.D. Argyle, C.H. Bartholomew, Heterogeneous catalyst deactivation and regeneration: a review, Catalysts 5 (2015) 145–269.
[87] A. Quintáns-Fondo, G. Ferreira-Coelho, M. Arias-Estévez, J.C. Nóvoa-Muñoz, D. Fernández-Calviño, E. Álvarez-Rodríguez, M.J. Fernández-Sanjurjo, A. Núñez-Delgado, Chromium VI and Fluoride Competitive Adsorption on Different Soils and By-Products, Processes 7 (2019) 748.
[88] N.B. Sanches, R. Pedro, M.F. Diniz, Ed.C. Mattos, S.N. Cassu, Rd.C.L. Dutra, Infrared spectroscopy applied to materials used as thermal insulation and coatings, J. Aerosp. Technol. Manag. 5 (2013) 421–430.
[89] P. Djinović, I.G. Osojnik Črnivec, B. Erjavec, A. Pintar, Influence of active metal loading and oxygen mobility on coke-free dry reforming of Ni–Co bimetallic catalysts, Appl. Catal. B: Environ. 125 (2012) 259–270.
[90] B.V. Ayodele, M.R. Khan, C.K. Cheng, Catalytic performance of ceria-supported cobalt catalyst for CO-rich hydrogen production from dry reforming of methane, Int. J. Hydrog. Energy 41 (2016) 198–207.
[91] S. Sang, Z.-J. Zhao, H. Tian, Z. Sun, H. Li, S. Assabumrungrat, T. Muhammad, L. Zeng, J. Gong, AIChE J. 66 (2020), e16877.
[92] M. Shokrollahi Yancheshmeh, M.C. Iliuta, A.C.S. Sustainable, Chem. Eng. 8 (2020) 16746–16756.